

Late Miocene Arctic warmth and terrestrial climate recorded by North Greenland speleothems

Received: 30 January 2025

Accepted: 15 September 2025

Published online: 21 October 2025

 Check for updates

Gina E. Moseley^{1,9}✉, Gabriella Koltai^{1,9}, Jonathan L. Baker^{1,9}, Jian Wang², Heather Stoll³, Anika Donner¹, Lena Friedrich¹, Christoph Spötl¹, M. Paul Smith⁴, Denis Scholz⁵, Hai Cheng², Adam Hartland⁶, Clivia Hejny⁷ & R. Lawrence Edwards⁸

The sensitivity of terrestrial Arctic climate during the Late Miocene remains poorly understood, despite this interval marking the transition towards a cooler, more variable global climate and the prelude to Northern Hemisphere glaciation. Here we present a Late Miocene terrestrial proxy record, developed through the analysis of speleothems, from eastern North Greenland (Kalaallit Nunaat). Growth periods indicate multiple episodes of permafrost absence between -10 and 5 Ma, suggesting mean annual air temperatures $\sim 14^\circ\text{C}$ higher than present coinciding with atmospheric CO_2 concentrations above ~ 310 ppm and local sea surface temperature anomalies $>2^\circ\text{C}$ higher than present. Such moderate thresholds for permafrost absence highlight the climate sensitivity of North Greenland. Spikes in siliciclastic-derived trace elements ~ 6.3 and ~ 5.6 Ma are interpreted as terrestrial indicators for Late Miocene ephemeral glaciers in North Greenland. Climate variability recorded during speleothem growth periods was predominantly forced by obliquity, although, in the earliest Late Miocene, obliquity-scale anti-phasing with Antarctica may have occurred. Regional sea-ice extent was at its greatest following ~ 5.6 Ma during phases of transient glacial–interglacial cycles. Our findings highlight the sensitivity of the Arctic climate system and permafrost to modest CO_2 levels and provide insights into regional responses to orbital forcing.

The Late Miocene (11.63 to 5.33 million years ago (Ma)) was characterized by global warmth relative to preindustrial values¹, superimposed on a cooling trend that became increasingly pronounced at high latitudes². Reconstructed atmospheric CO_2 concentrations of ~ 200 – 500 ppm (refs. 3,4) encompass current values and near-future projections, during a time when global palaeogeography was approaching its modern configuration^{5,6}. The Late Miocene therefore provides important insights into climate forcings, feedbacks and variability relevant to long-term outcomes of modern climate scenarios².

Despite its importance for predicting near-future global change², knowledge of Late Miocene Arctic climate variability is limited by scarce terrestrial proxy records. Arctic terrestrial palaeoreconstructions and interpretations rely predominantly on glacial geomorphology^{7–11}, marine records^{7,12–17} and numerical modelling⁹. Northern Hemisphere high-latitude cooling during the Late Miocene is linked to CO_2 decline, along with palaeogeographic and vegetation changes^{2,18,19}. However, high-resolution climate records remain scarce, yet they are crucial for validating future climate scenarios and understanding Arctic boundary

A full list of affiliations appears at the end of the paper. ✉ e-mail: gina.moseley@uibk.ac.at

conditions before Northern Hemisphere glaciations²⁰. Greenland is thus a priority for acquiring new proxy data²¹ in order to validate model outputs^{21,22}.

This study addresses critical knowledge gaps in terrestrial High Arctic Late Miocene temperature, glacial and permafrost evolution, in addition to orbital forcing of climate and sea-ice variability. Precise, radiometrically dated speleothem growth periods from eastern North (eN.) Greenland provide unambiguous evidence for episodes of permafrost absence between -10 and 5 Ma. These growth periods align to elevated sea surface temperatures (SSTs) in the northern North Atlantic^{5,18,20} and only moderate atmospheric CO₂ levels^{3,4}. Reproducible multi-proxy time series suggest orbital forcing of temperature and sea-ice extent, alongside terrestrial evidence of Late Miocene glaciation in North Greenland.

Geological and field setting

Four flowstone speleothems were sampled from the rear of Cove Cave (Eqik Qaarusussuaq; 80.3° N, 21.9° W (ref. 23); Fig. 1 and Extended Data Figs. 1 and 2) in eN.Greenland, ~35 km west of the coast and ~60 km northeast of the Greenland ice sheet (Fig. 1). Currently, the plateau above the cave lacks an ice cap, although one existed in 1983. In 1889, rapid surface melting caused water to enter the cave, freeze and form cryogenic cave minerals²⁴, as occurs when cave air temperature remains below freezing (that is, in permafrost).

The cave, located ~660 m above sea level (asl) and ~30 m below the plateau surface, lies within a tributary valley connected to a steep-sided canyon (Extended Data Fig. 1). Quaternary fluvial incision truncated the cave, leaving it shorter than during speleothem growth.

Modern arid conditions (~200 mm per year (ref. 25) and continuous permafrost²⁶ limit water infiltration into the cave, therefore preventing vadose speleothem formation. Patterned ground and cryptobiotic soils are scarce on the plateaus but present in valley bottoms (Extended Data Fig. 1). The mean annual air temperature (MAAT; 1991–2020) of -13.7 ± 1.0 °C at the cave location is consistent with spot cave air measurements of -14 °C recorded at the sampling site²³ (Extended Data Fig. 2). Only 3 months per annum were above freezing, and a warming trend of 0.9 ± 0.1 °C per decade has been recorded (Extended Data Fig. 3).

Radiometrically dated speleothem growth

The speleothems (code KC) consist primarily of brown calcite, except for a distinctive, thin white layer that is macroscopically, microscopically and geochemically consistent across all samples (Extended Data Fig. 4). Stable-isotope profiles of $\delta^{18}\text{O}$ and $\delta^{13}\text{C}$ are reproducible throughout the entire common record, enabling a stacked composite record (Extended Data Fig. 5). The only exception is the base of KC19–14, which extends further back in time. Given the strong reproducibility in the younger section of the record, we also regard the older part of KC19–14 as reliable, although not yet replicated.

U-series (U–Th and U–Pb) dating and Bayesian age modelling of the KC samples indicate four depositional phases: -9.5–9.3, -8.1–7.8, -6.3–6.1 and -5.6–5.3 Ma, with a possible brief interval -7.2 Ma (Fig. 2, Extended Data Fig. 6, Supplementary Discussions 1 and 2 and Supplementary Table 1). The mean uncertainty across the age model is 0.8% (standard deviation 0.5, range 0.01–2.6%). However, preliminary U–Pb ages from another cave in the region (15 km northeast) indicate that deposition may have continued between 9.3 and 8.1 Ma, indicating this hiatus is not widespread (Fig. 2). Moreover, speleothem growth in the Siberian Arctic 2,000 km to the south²⁷ (72° N; Fig. 2) occurred 8.68 ± 0.09 Ma. Given the preliminary ages from our other field site, we do not continue with a detailed proxy interpretation for this particular sample, but consider growth to have been more or less continuous between -9.5 and 7.8 Ma (Fig. 2). Hiatuses 1 and 2 occurred between -7.8 and 6.3 and -6.1 and 5.6 Ma, respectively, with final growth ending at -5.3 Ma near the Miocene–Pliocene boundary (Fig. 2). We rule

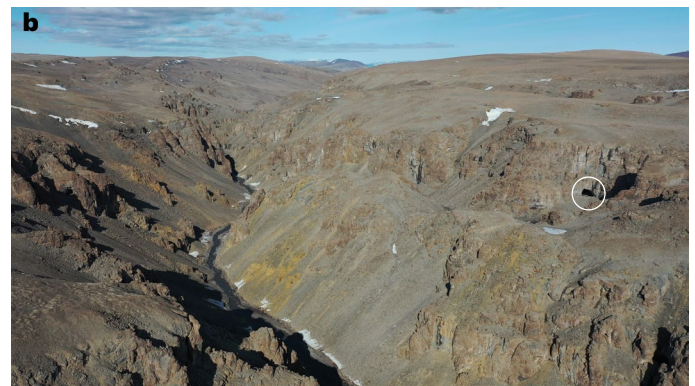


Fig. 1 | Field location of Cove Cave (Eqik Qaarusussuaq)²³ relative to other sites discussed in the text. a, Present coastlines (blue outline) and country boundaries (brown lines), palaeo-land masses at 8 Ma (ref. 6) (green), studied cave location (red circle) and various marine records (black squares). **b**, A photograph of the landscape with the studied cave entrance inside the white circle. Credit: **b**, Robbie Shone. See Extended Data Fig. 1 for further details.

out Quaternary growth at this site (Supplementary Discussion 2), but acknowledge possible short-lived episodes in eN.Greenland based on evidence from other Northern Hemisphere high-latitude sites^{28–30}.

Climatic drivers of speleothem growth

Speleothem deposition during the Late Miocene at -9.5–7.8, -6.3–6.1 and -5.6–5.3 Ma indicates a more humid climate with ground and cave-air temperatures above 0 °C, implying the absence of permafrost. Regular fluorescent lamination (Extended Data Fig. 7) indicates soil and vegetation were above the cave throughout all depositional phases³¹, whereas speleothem $\delta^{13}\text{C}$ values below those of the local limestone bedrock (-0.1 ± 0.1 ‰; Extended Data Fig. 5) further exclude growth in a subglacial environment or barren snowscape³¹. While higher Late Miocene precipitation³² could have enhanced winter ground insulation (Supplementary Discussion 3), this effect is likely to be offset by a longer warm season. We therefore suggest that the MAAT was above freezing during speleothem growth phases, indicating it was at least 13.7 ± 1.0 °C higher than the 1991–2020 mean.

Comparison of the speleothem growth phases with SST anomalies indicates that deposition occurred when SSTs exceeded modern values by >8 °C in the northern North Atlantic (ODP Site 982)^{5,18} and >6 °C in the Iceland Sea (ODP Site 907)^{18,20} (Fig. 2). Considering a persistent

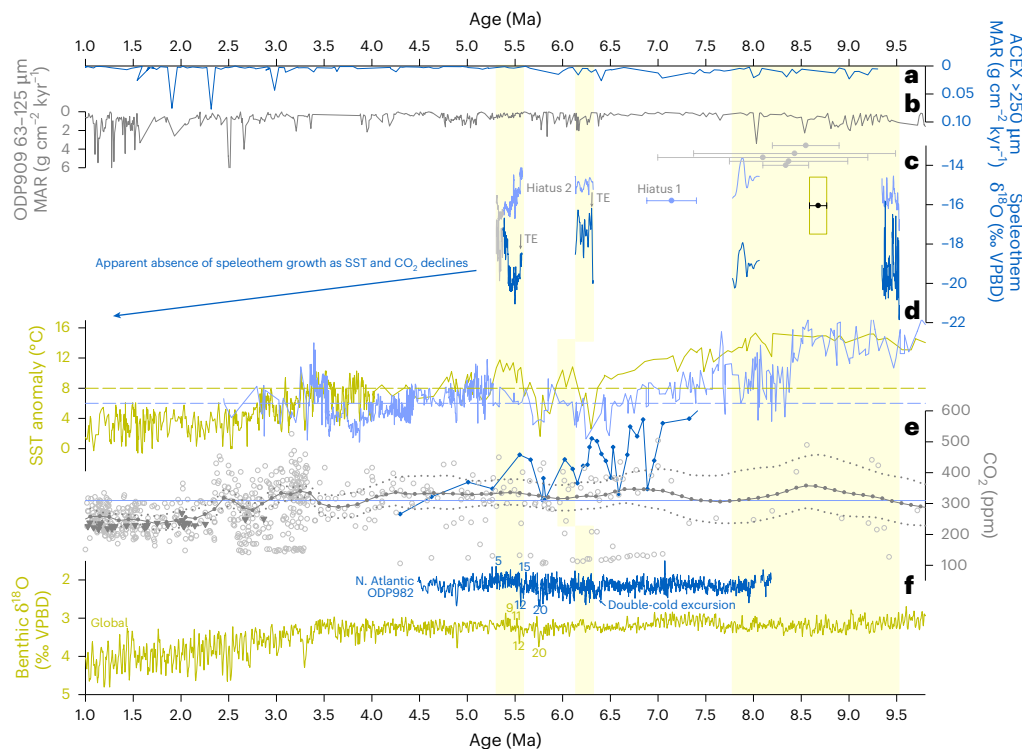


Fig. 2 | Eastern North Greenland speleothem time series compared with other proxies over the interval 1–9.8 Ma. **a**, Mean accumulation rate (MAR) of >250- μm fraction at the central Arctic ACEX site¹⁵. **b**, MAR of 63–125- μm fraction at ODP Site 909 in the Fram Strait^{17,33}. **c**, U–Pb ages for other caves discussed in the text (grey circles), with uncertainties shown as means and propagated 2 standard error bars. Individual statistics given in Supplementary Table 1). Eastern North Greenland original speleothem $\delta^{18}\text{O}$ composite curve (light blue, this study) and prior calcite precipitation (PCP)-corrected speleothem $\delta^{18}\text{O}$ composite curve (medium blue, this study). Less reliable age model (grey, this study) and singular age (light-blue circle, 2 σ ; Supplementary Discussion 2). Siberian speleothem age and uncertainty (black circle, 2 σ) surrounded by its

$\delta^{18}\text{O}$ range (open yellow box)²⁷. TE indicates the position of trace element spikes. **d**, Sea surface temperature (SST) anomalies ($U_{k_{37}}^{\text{K}}$) relative to modern at ODP Site 982 (yellow) and ODP Site 907 (blue)¹⁸. Horizontal dashed lines highlight thresholds above which speleothem deposition occurred. **e**, Community-vetted atmospheric CO_2 records (circles) with 100-kyr mean statistical reconstructions shown as median (grey solid) and 95% credible intervals (grey dotted)^{3,4}. Antarctic ice CO_2 (grey triangles)³⁵ and high-resolution S. Atlantic $p\text{CO}_2$ record (blue circles)³⁶. CO_2 threshold above which speleothem growth occurred (blue horizontal line). **f**, Benthic $\delta^{18}\text{O}$ ODP Site 982^{37,39} (blue) and global stack⁴⁹ (yellow). Numbers refer to marine oxygen isotope stratigraphy⁴⁰. Vertical yellow bars highlight speleothem growth periods.

-5 °C SST offset between ODP Site 907 and the central Arctic (ACEX) during the Late Miocene²⁰, similar to today¹⁸. SSTs in the Arctic Gateway near our field site were probably -3–4 °C cooler than at ODP Site 907¹⁸. Accordingly, based on current understanding of North Atlantic SST knowledge and chronologies, speleothem deposition probably occurred when local SST anomalies in the Arctic Gateway exceeded 2–3 °C above modern values. Interestingly, SSTs during hiatus 1 also occasionally exceeded this threshold. While this could reflect sampling bias, a major reorganization of ocean circulation in the Arctic Gateway around -7.5 Ma, related partly to strengthening of the Atlantic Meridional Overturning Circulation and the North Atlantic Current³³, may have triggered regional climate changes that led to a cessation of speleothem growth.

Critically, community-vetted atmospheric CO_2 estimates^{3,4} indicate that periods of eN.Greenland speleothem growth occurred at CO_2 levels above 310 +96/-73 ppm, thereby supporting elevated temperatures at only moderate CO_2 concentrations³⁴. Notably, periods of growth cessation also occurred above this CO_2 concentration (Fig. 2). However, large scatter, limited variability and sparse early Late Miocene CO_2 data hinder a thorough assessment of speleothem growth in relation to CO_2 forcing. Evidence from Pliocene-age Antarctic ice³⁵ now confirms that past CO_2 levels were on the lower end of marine-based reconstructions (Fig. 2). This suggests that hiatuses in speleothem growth may have coincided with periods of reduced CO_2 concentrations. This is supported by a high-resolution $p\text{CO}_2$ reconstruction from the South Atlantic that spans the Late Miocene Cooling³⁶. Although

this record generally shows elevated CO_2 concentrations compared with other records, high-frequency CO_2 variability is observed across the Late Miocene Cooling with distinctive drops in CO_2 during both hiatuses 1 and 2 (Fig. 2).

Regardless of the CO_2 record that is chosen, modern atmospheric CO_2 concentrations have now surpassed thresholds that in the Late Miocene enabled speleothem growth. Over recent years (1991–2020), eN.Greenland has warmed at 0.9 ± 0.1 °C per decade. Sea ice in the Arctic gateway is also at a record low, thereby leading to reduced ice–albedo feedbacks that are important for permafrost stability²⁹. It is therefore possible that the region has already surpassed a tipping point. If warming continues to an equilibrium state where sea surface temperatures in the Arctic Gateway reach 2–3 °C above modern levels, evidence from the speleothem record and current warming rates suggest that complete permafrost thaw in the upper tens of metres could occur within the next one to two centuries. This is in line with predictions for summer sea-ice loss in the Arctic Ocean²⁰.

Late Miocene glacial expansion

The cessation of speleothem deposition during hiatuses 1 and 2 (Fig. 2) may be attributed to preservation or sampling biases; however, the timing of these hiatuses suggests that regional cooling and/or aridification probably inhibited speleothem growth. Marine records from these intervals indicate substantial changes in both surface^{5,18,20} and deep ocean³³ conditions (Fig. 2). Notably, North Atlantic SSTs declined during the Late Miocene^{5,18} with enhanced high-latitude cooling during

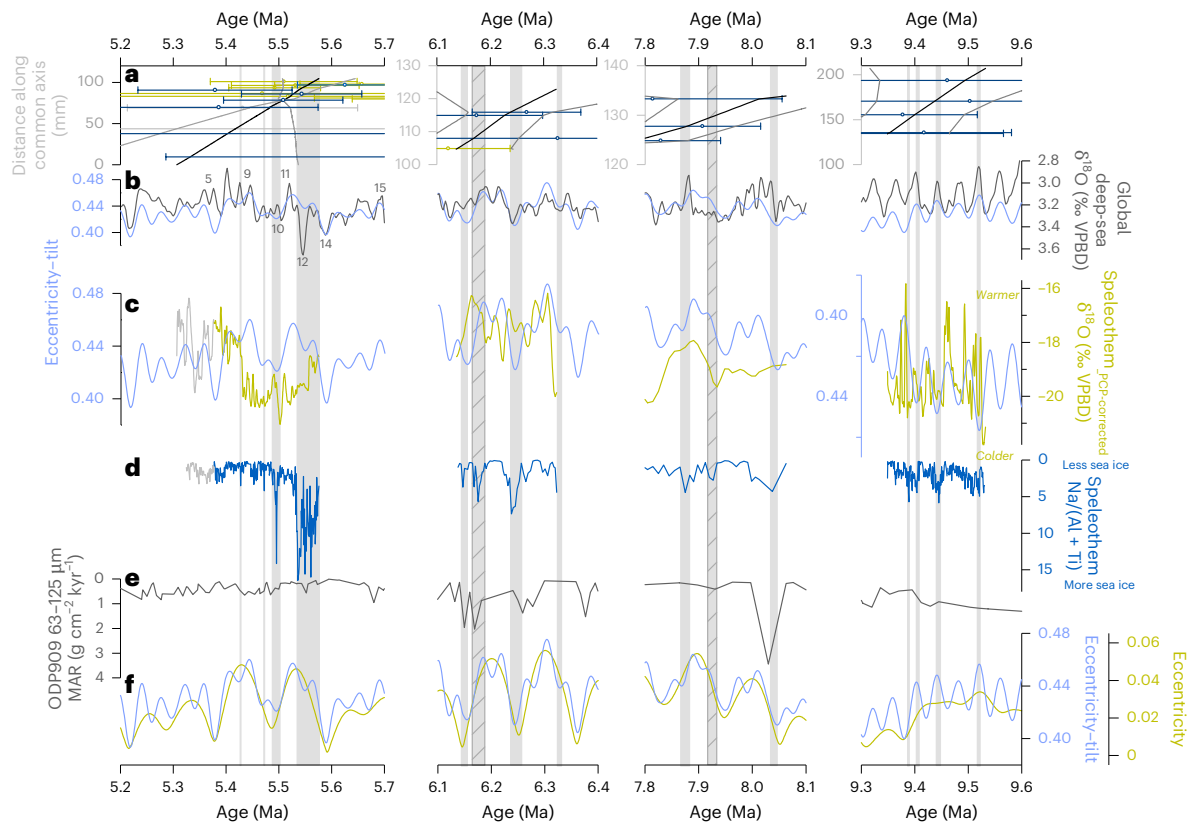


Fig. 3 | Time-series of periods of eastern North Greenland speleothem deposition. **a**, U–Pb ages (horizontal bars are uncertainties plotted as mean and propagated 2 standard error uncertainty. Individual statistics given in Supplementary Table 1) and Bayesian age model (centre age in black, 95% confidence in grey) as described in text. KC19-7 (yellow), KC19-9 (medium blue), KC19-12 (grey), KC19-14 (dark blue). **b**, Global benthic $\delta^{18}\text{O}$ stack⁴⁹ (grey). Numbers highlight ‘TG’ marine isotope stratigraphy⁴⁰. **c**, Eastern North Greenland PCP-corrected $\delta^{18}\text{O}$ composite curve (yellow). **d**, Eastern North Greenland Na/(Al + Ti) record (blue; this study). **e**, Mean accumulation rate (MAR) of 63–125- μm fraction at ODP Site 909 in the Fram Strait^{17,33}. **f**, Orbital eccentricity⁴⁸ (yellow) and eccentricity–tilt composite^{47,48} (blue). Vertical grey bars highlight sea-ice expansion events. Solid bars align with obliquity nodes, while hatched bars indicate sea-ice expansion events associated with alternative orbital forcing.

curve (yellow). Less reliable age model (grey) (Supplementary Discussion 2; this study). Eccentricity–tilt composite^{47,48} (blue). **d**, Eastern North Greenland Na/(Al + Ti) record (blue; this study). Less reliable age model (grey) (Supplementary Discussion 2). **e**, Mean accumulation rate (MAR) of 63–125- μm fraction at ODP Site 909 in the Fram Strait^{17,33}. **f**, Orbital eccentricity⁴⁸ (yellow) and eccentricity–tilt composite^{47,48} (blue). Vertical grey bars highlight sea-ice expansion events. Solid bars align with obliquity nodes, while hatched bars indicate sea-ice expansion events associated with alternative orbital forcing.

hiatus 1 (ref. 5). Furthermore, two major SST collapses¹⁸ occurred during hiatuses 1 and 2, falling below temperature thresholds required for speleothem formation (Fig. 2). After the final growth cessation, SST and CO_2 levels remained consistently below these thresholds throughout much of the Pliocene and Quaternary. This prolonged cooling trend likely promoted permafrost development, explaining the absence of speleothem deposition during these later intervals (Fig. 2).

Although there is a slight offset between the ~6.3–6.1 Ma speleothem growth phase and the peak in regional SST, the pattern and duration of SST variability are broadly consistent with speleothem growth, suggesting the offset may be due to chronological uncertainty (Fig. 2). As SSTs declined during the growth hiatuses, eN.Greenland MAAT likely dropped as well, potentially promoting permafrost aggradation and halting speleothem formation. Northern North Atlantic benthic $\delta^{18}\text{O}$ (ODP Site 982) records a double cold excursion (~0.7‰) between ~6.4 and 6.3 Ma (ref. 37), coinciding with the first SST collapse¹⁸ and the end of hiatus 1. Hiatus 2 aligns with extensive Antarctic ice expansion³⁸ as well as a series of transient glacial–interglacial cycles in which the most prominent was TG20^{39,40}.

Deep-ocean records from the nearby Fram Strait (ODP Site 909) show ice-rafted debris^{17,33} (IRD) during hiatus 2, while ACEX¹⁵ contains IRD during both hiatuses (Fig. 2). Quartz grains with glacial microtextures are also found at ACEX around ~7.0, ~6.0 and ~5.5 Ma (ref. 41). Farther south, dropstones off central East Greenland (ODP Site 987) indicate IRD deposition began ~7.5 Ma (ref. 14), with episodic IRD from central East Greenland reaching offshore South-East Greenland (ODP Site 918) by ~7 Ma (ref. 13). There is thus substantial evidence

for ocean-terminating glaciers on Greenland during hiatuses 1 and 2. IRD provenance¹³, geomorphological and modelling studies^{8,9,42} all suggest that Late Miocene glaciation was confined to the higher elevations of South-East, southern East, and central Greenland. However, following hiatus 1, all speleothem samples exhibit a distinct white calcitic layer (Fig. 2 and Extended Data Fig. 4) marked by abrupt increases in siliclastic-derived trace elements (Extended Data Fig. 8). A smaller spike of the same composition is also present following hiatus 2. The elemental signature falls between local carbonate bedrock and recently eroded silicate material from glacial outwash sites (Extended Data Fig. 9) on Precambrian sequences of the former Caledonian highlands (~10 km away). The trace element spikes following hiatuses 1 and 2 are therefore considered to capture the chemical imprint of ice retreat. While the full extent of these glaciations remains uncertain, this represents a terrestrial indication of Late Miocene glacial expansion in eN.Greenland. Our speleothem record supports modelling studies suggesting substantial glacial expansion also occurred in North Greenland during the Late Miocene¹¹. In the model, ice responded sensitively to temperature variability but formed rapidly under cold conditions¹¹; we therefore suspect a glaciation occurred near the end of hiatus 1, probably at the time of the North Atlantic ‘double cold excursion’³⁷, the first distinctive drop in SST¹⁸ and IRD at the ACEX site¹⁵.

Orbital forcing, sea-ice extent and hemispheric phasing

Speleothem $\delta^{18}\text{O}$ time series have been corrected to account for the maximum potential $\delta^{18}\text{O}$ enrichment from prior calcite precipitation

(PCP)³¹ (Extended Data Fig. 10; Supplementary Discussion 4). The original (climate-driven) $\delta^{18}\text{O}$ signal of groundwater bicarbonate therefore lies between the measured and PCP-corrected extremes. Regardless of the absolute values, the resulting variability appears robust across a range of model parameters, and the PCP-corrected record restores higher-amplitude $\delta^{18}\text{O}$ shifts and oscillations muted in the original data. This variability forms the basis of the discussion, and we interpret the trends as reliable indicators of isotopic variability driven by regional climate change (Fig. 3). Because regional uplift ceased before speleothem deposition^{11,43}, elevation changes are unlikely to have influenced the $\delta^{18}\text{O}$ signal. In addition, as used in polar ice core studies⁴⁴, Na was analysed as a proxy for the sea-salt component of marine aerosols (Supplementary Discussion 5). On Greenland's east coast, Na primarily derives from sea-ice surfaces^{45,46}, with elevated concentrations indicating greater sea-ice extent⁴⁵. To isolate the marine aerosol signal (Na_{ss}), Na was normalized to the siliciclastic elements Al and Ti, accounting for minor mineral dust contributions⁴⁶ (Fig. 3). The fluctuating sea-ice cover recorded in the speleothems thus aligns with Late Miocene Arctic Ocean biomarkers, which indicate irregular spring sea ice and ice-free summers²⁰.

The following discussion into the timing of climatic variability utilizes the independent, radiometrically dated age-modelled chronology. Nonetheless, we acknowledge the age uncertainties and recognize that further research is needed to draw more definitive conclusions.

As noted elsewhere, obliquity forcing played a dominant role in Late Miocene climate variability^{2,37,47}. While speleothem $\delta^{18}\text{O}$ variability during all growth phases generally reflects orbital pacing, we observe that the relationship is especially pronounced during the low-amplitude eccentricity cycles between -9.6 and 9.3 Ma (Fig. 3), consistent with previous observations⁴⁷. On this particular chronology, however, the relationship between $\delta^{18}\text{O}$ and orbital forcing appears inverted when compared with other growth periods. Specifically, higher $\delta^{18}\text{O}$ values (warmer temperatures), correlate with low eccentricity-tilt^{47,48} and increased benthic $\delta^{18}\text{O}$ indicating greater ice volume. Na_{ss} is generally low throughout the growth phase, but increases occasionally with temperature declines. The orbitally tuned global benthic $\delta^{18}\text{O}$ record⁴⁹ naturally shows a clear relationship with eccentricity-tilt across all phases (Fig. 3). However, between -9.6 and 9.3 Ma, the ice volume signal in the benthic $\delta^{18}\text{O}$ record reflects only Antarctic contributions⁴⁷, whereas later growth periods may incorporate Northern Hemisphere ice as well. This -9.6–9.3 Ma interval was also marked by enhanced North Atlantic poleward heat transport and a collapsed meridional temperature gradient, which reestablished before subsequent growth phases⁵. During this time, speleothem $\delta^{18}\text{O}$ suggests hemispheric anti-phasing, with Antarctic ice expanding during intervals of elevated Arctic temperatures (and vice versa; Fig. 3). After -8 Ma, following reestablishment of the North Atlantic temperature gradient⁵ and the onset of ephemeral Northern Hemisphere glaciations, a closer alignment between speleothem $\delta^{18}\text{O}$ and global benthic $\delta^{18}\text{O}$ (ref. 49) indicates that the two hemispheres operated more in-phase.

If the observed hemispheric anti-phasing and the inverse relationship between temperature and orbital forcing in the Arctic are accurate, they may have been partly driven by vegetation feedbacks, which played a key role in Late Miocene climate^{1,19}. Over the past 12 Ma, Arctic forest canopy density peaked -9.7 Ma, after which it became increasingly open, dominated by shrubs and herbs⁵⁰. During the first speleothem growth phase, surface albedo was at its lowest, enhancing latent heat flux and atmospheric water vapour through increased evapotranspiration, contributing to elevated temperatures¹⁹. Despite weaker summer radiative forcing during low eccentricity-tilt phases, a longer warm season would have enabled positive vegetation feedbacks to persist over an extended period. As Arctic climate cooled through the Late Miocene, vegetation became more open¹⁹, the North Atlantic meridional temperature gradient increased⁵ and both Atlantic Meridional Overturning Circulation and North Atlantic Current

strengthened³³. This transition marked a shift towards a regime of transient glacial–interglacial cycles in the Arctic, operating in-phase with Antarctic ice sheet variability under shared orbital controls. High speleothem $\delta^{18}\text{O}$ values generally coincided with high eccentricity-tilt and stronger summer seasonality, whereas low eccentricity-tilt facilitated sea-ice expansion.

The greatest sea-ice extent occurred during the final growth phase beginning -5.57 Ma. During the preceding hiatus, the pronounced TG20 glacial occurred. The glacial cycles that followed were less extreme, and by interglacial TG15, Antarctic ice volume dropped sharply³⁸. Glacial TG14 appears to have been a relatively minor glacial, and as it ended, speleothem deposition resumed despite elevated Na_{ss} levels indicating substantial sea-ice extent (Fig. 3). Sea ice may therefore have been present in the Arctic Ocean, even during the summer months, consistent with a moderately elevated CO_2 scenario²⁰. The sea ice remained, displaying high-amplitude high-frequency oscillations until -5.53 Ma, then rapidly disappeared during the TG12 deglacial (Fig. 3). It expanded again for a short time during TG10, reaching peak expansion at the obliquity node. From -5.49 to 5.38 Ma, Na_{ss} indicates persistently low sea ice with minor expansions, matching limited deep-sea $\delta^{18}\text{O}$ variability^{37,39,49}. At -5.43 Ma, a rapid $\delta^{18}\text{O}$ increase aligns with interglacial TG9⁴⁰, paralleling rapid Antarctic deglaciation³⁸.

Together, the $\delta^{18}\text{O}$ and Na_{ss} time series reveal that eN.Greenland experienced pronounced Late Miocene climate and sea-ice variability. Clear connections to orbital forcing are difficult to reconcile within the limits of the chronology; however, it is clear that Late Miocene Arctic climate was much more dynamic and transient than has been captured thus far by modelling studies that are often limited to specific time slices and CO_2 boundary conditions.

Online content

Any methods, additional references, Nature Portfolio reporting summaries, source data, extended data, supplementary information, acknowledgements, peer review information; details of author contributions and competing interests; and statements of data and code availability are available at <https://doi.org/10.1038/s41561-025-01822-0>.

References

1. Pound, M. J., Haywood, A. M., Salzmann, U. & Riding, J. B. Global vegetation dynamics and latitudinal temperature gradients during the Mid to Late Miocene (15.97–5.33Ma). *Earth Sci. Rev.* **112**, 1–22 (2012).
2. Steinhorsdottir, M. et al. The Miocene: the future of the past. *Paleoceanogr. Paleoclimatol.* **36**, e2020PA004037 (2021).
3. The Cenozoic CO_2 proxy integration project (CenCO2PIP). Toward a Cenozoic history of atmospheric CO_2 . *Science* **382**, eadi5177 (2023).
4. The CenCO2PIP consortium. Data Product for "Toward a Cenozoic history of atmospheric CO_2 ": Dataset V1.02. *Zenodo* <https://doi.org/10.5281/zenodo.14537923> (2024).
5. Super, J. R. et al. Miocene evolution of North Atlantic sea surface temperature. *Paleoceanogr. Paleoclimatol.* **35**, e2019PA003748 (2020).
6. Markwick, P. J. in *Deep-Time Perspectives on Climate Change: Marrying the Signal from Computer Models and Biological Proxies* (eds Williams, M. et al.) 251–312 (Geological Society of London, 2007).
7. Bierman, P. R., Shakun, J. D., Corbett, L. B., Zimmerman, S. R. & Rood, D. H. A persistent and dynamic East Greenland Ice Sheet over the past 7.5 million years. *Nature* **540**, 256–260 (2016).
8. Pedersen, V. K., Larsen, N. K. & Egholm, D. L. The timing of fjord formation and early glaciations in North and Northeast Greenland. *Geology* **47**, 682–686 (2019).
9. Paxman, G. J. G., Jamieson, S. S. R., Dolan, A. M. & Bentley, M. J. Subglacial valleys preserved in the highlands of south and east Greenland record restricted ice extent during past warmer climates. *Cryosphere* **18**, 1467–1493 (2024).

10. Bonow, J. M. & Japsen, P. Penneplains and tectonics in North-East Greenland after opening of the North-East Atlantic. *GEUS Bull.* **45**, 5297 (2021).
11. Solgaard, A. M., Bonow, J. M., Langen, P. L., Japsen, P. & Hvidberg, C. S. Mountain building and the initiation of the Greenland Ice Sheet. *Palaeogeogr. Palaeoclimatol. Palaeoecol.* **392**, 161–176 (2013).
12. Moran, K. et al. The Cenozoic palaeoenvironment of the Arctic Ocean. *Nature* **441**, 601–605 (2006).
13. Larsen, H. C. et al. Seven million years of glaciation in Greenland. *Science* **264**, 952–955 (1994).
14. Butt, F. A., Elverhøi, A., Forsberg, C. F. & Solheim, A. Evolution of the Scoresby Sund Fan, central East Greenland—evidence from ODP Site 987. *Norw. J. Geol.* **81**, 3–15 (2001).
15. St. John, K. Cenozoic ice-rafting history of the central Arctic Ocean: Terrigenous sands on the Lomonosov Ridge. *Paleoceanography* **23**, PA1S05 (2008).
16. Thiede, J. et al. Millions of years of Greenland ice sheet history recorded in ocean sediments. *Polarforschung* **80**, 141–159 (2011).
17. Wolf-Welling, T. C. W., Cremer, M., O’Connell, S., Winkler, A. & Thiede, J. Cenozoic Arctic gateway paleoclimate variability: Indications from changes in coarse-fraction composition. In *Proc. Ocean Drilling Program Scientific Results*, Vol 151 (eds Thiede, J. et al.) 515–567 (1996).
18. Herbert, T. D. et al. Late Miocene global cooling and the rise of modern ecosystems. *Nat. Geosci.* **9**, 843–847 (2016).
19. Zhang, R. et al. Vegetation feedbacks accelerated the late Miocene climate transition. *Sci. Adv.* **11**, eads4268 (2025).
20. Stein, R. et al. Evidence for ice-free summers in the late Miocene central Arctic Ocean. *Nat. Commun.* **7**, 11148 (2016).
21. Lunt, J. D. et al. A methodology for targeting palaeo proxy data acquisition: a case study for the terrestrial late Miocene. *Earth Planet. Sci. Lett.* **271**, 53–62 (2008).
22. Hossain, A. et al. The impact of different atmospheric CO₂ concentrations on large scale Miocene temperature signatures. *Paleoceanogr. Paleoclimatol.* **38**, e2022PA004438 (2023).
23. Moseley, G. E. et al. Cave discoveries and speleogenetic features in northeast Greenland. *Cave Karst Sci.* **47**, 74–87 (2020).
24. Donner, A. et al. Cryogenic cave minerals recorded the 1889 CE melt event in northeastern Greenland. *Clim. Past* **19**, 1607–1621 (2023).
25. Schuster, L., Maussion, F., Langhamer, L. & Moseley, G. E. Lagrangian detection of precipitation moisture sources for an arid region in northeast Greenland: relations to the North Atlantic Oscillation, sea ice cover, and temporal trends from 1979 to 2017. *Weather Clim. Dyn.* **2**, 1–17 (2021).
26. Obu, J. et al. Northern Hemisphere permafrost map based on TTOP modelling for 2000–2016 at 1 km² scale. *Earth Sci. Rev.* **193**, 299–316 (2019).
27. Umbo, S. et al. Speleothem evidence for late Miocene extreme Arctic amplification—an analogue for near future anthropogenic climate change? *Clim. Past* **21**, 1533–1551 (2025).
28. Moseley, E. G., Edwards, L. R., Lord, S. N., Spötl, C. & Cheng, H. Speleothem record of mild and wet mid-Pleistocene climate in northeast Greenland. *Sci. Adv.* **7**, eabe1260 (2021).
29. Vaks, A. et al. Palaeoclimate evidence of vulnerable permafrost during times of low sea ice. *Nature* **577**, 221–225 (2020).
30. Batchelor, J. C. et al. Insights into changing interglacial conditions in subarctic Canada from MIS 11 through MIS 5e from seasonally resolved speleothem records. *Geophys. Res. Lett.* **51**, e2024GL108459 (2024).
31. Skiba, V., Juvet, G., Marwan, N., Spötl, C. & Fohlmeister, J. Speleothem growth and stable carbon isotopes as proxies of the presence and thermodynamical state of glaciers compared to modelled glacier evolution in the Alps. *Quat. Sci. Rev.* **322**, 108403 (2023).
32. Schubert, B. A., Jahren, A. H., Davydov, S. P. & Warny, S. The transitional climate of the late Miocene Arctic: winter-dominated precipitation with high seasonal variability. *Geology* **45**, 447–450 (2017).
33. Gruetzner, J., Matthiessen, J., Geissler, W. H., Gebhardt, A. C. & Schreck, M. A revised core-seismic integration in the Molloy Basin (ODP Site 909): implications for the history of ice rafting and ocean circulation in the Atlantic–Arctic gateway. *Glob. Planet. Change* **215**, 103876 (2022).
34. Knorr, G., Butzin, M., Micheels, A. & Lohmann, G. A warm Miocene climate at low atmospheric CO₂ levels. *Geophys. Res. Lett.* **38**, L20701 (2011).
35. Marks Peterson, M. J. et al. Ice cores from the Allan Hills, Antarctica show relatively stable atmospheric CO₂ and CH₄ levels over the last 3 million years. Preprint at *Research Square* <https://doi.org/10.21203/rs.3.rs-5610566/v1> (2024).
36. Tanner, T., Hernández-Almeida, I., Drury, A. J., Guitián, J. & Stoll, H. Decreasing atmospheric CO₂ during the Late Miocene Cooling. *Paleoceanogr. Paleoclimatol.* **35**, e2020PA003925 (2020).
37. Drury, A. J., Westerhold, T., Hodell, D. & Röhl, U. Reinforcing the North Atlantic backbone: revision and extension of the composite splice at ODP Site 982. *Clim. Past* **14**, 321–338 (2018).
38. Ohneiser, C. et al. Antarctic glacio-eustatic contributions to late Miocene Mediterranean desiccation and reflooding. *Nat. Commun.* **6**, 8765 (2015).
39. Hodell, D. A., Curtis, J. H., Sierro, F. J. & Raymo, M. E. Correlation of Late Miocene to Early Pliocene sequences between the Mediterranean and North Atlantic. *Paleoceanography* **16**, 164–178 (2001).
40. Shackleton, N., Hall, M. A. & Pate, D. Pliocene stable isotope stratigraphy of site 846. *Proc. Ocean Drilling Program, Scientific Results*, Vol 138, 337–355 (1995).
41. Immonen, N. Surface microtextures of ice-rafted quartz grains revealing glacial ice in the Cenozoic Arctic. *Palaeogeogr. Palaeoclimatol. Palaeoecol.* **374**, 293–302 (2013).
42. Pérez, F. L., Nielsen, T., Knutz, C. P., Kuijpers, A. & Damm, V. Large-scale evolution of the central-east Greenland margin: new insights to the North Atlantic glaciation history. *Glob. Planet. Change* **163**, 141–157 (2018).
43. Japsen, P., Green, P. F., Chalmers, J. A. & Bonow, J. M. Episodes of post-Caledonian burial and exhumation in Greenland and Fennoscandia. *Earth Sci. Rev.* **248**, 104626 (2024).
44. Wolff, E. W. et al. Southern Ocean sea-ice extent, productivity and iron flux over the past eight glacial cycles. *Nature* **440**, 491–496 (2006).
45. Rhodes, R. H., Yang, X. & Wolff, E. W. Sea ice versus storms: what controls sea salt in Arctic ice cores?. *Geophys. Res. Lett.* **45**, 5572–5580 (2018).
46. Maffezzoli, N. et al. Sea ice in the northern North Atlantic through the Holocene: evidence from ice cores and marine sediment records. *Quat. Sci. Rev.* **273**, 107249 (2021).
47. Holbourn, A., Kuhnt, W., Clemens, S., Prell, W. & Andersen, N. Middle to late Miocene stepwise climate cooling: evidence from a high-resolution deep water isotope curve spanning 8 million years. *Paleoceanography* **28**, 688–699 (2013).
48. Laskar, J. et al. A long-term numerical solution for the insolation quantities of the Earth. *Astron. Astrophys.* **428**, 261–285 (2004).
49. Westerhold, T. et al. An astronomically dated record of Earth’s climate and its predictability over the last 66 million years. *Science* **369**, 1383–1387 (2020).
50. Zhang, J. et al. Evolutionary history of the Arctic flora. *Nat. Commun.* **14**, 4021 (2023).

Publisher’s note Springer Nature remains neutral with regard to jurisdictional claims in published maps and institutional affiliations.

Open Access This article is licensed under a Creative Commons Attribution 4.0 International License, which permits use, sharing, adaptation, distribution and reproduction in any medium or format, as long as you give appropriate credit to the original author(s) and the source, provide a link to the Creative Commons licence, and indicate if changes were made. The images or other third party material in this article are included in the article's Creative Commons licence, unless indicated otherwise

in a credit line to the material. If material is not included in the article's Creative Commons licence and your intended use is not permitted by statutory regulation or exceeds the permitted use, you will need to obtain permission directly from the copyright holder. To view a copy of this licence, visit <http://creativecommons.org/licenses/by/4.0/>.

© The Author(s) 2025

¹Institute of Geology, University of Innsbruck, Innsbruck, Austria. ²Institute of Global Environmental Change, Xi'an Jiaotong University, Xi'an, China. ³Department of Earth Sciences, ETH Zürich, Zurich, Switzerland. ⁴Oxford University Museum of Natural History, Oxford, UK. ⁵Institute for Geosciences, Johannes Gutenberg University Mainz, Mainz, Germany. ⁶Te Aka Mātuatua, School of Science, University of Waikato, Hamilton, New Zealand. ⁷Institute of Mineralogy and Petrography, University of Innsbruck, Innsbruck, Austria. ⁸School of Earth and Environmental Sciences, University of Minnesota, Minneapolis, MN, USA. ⁹These authors contributed equally: Gina E. Moseley, Gabriella Koltai, Jonathan L. Baker. ✉e-mail: gina.moseley@uibk.ac.at

Methods

Geographical divisions

In this study, geographical subdivisions as defined by the Geological Survey of Denmark and Greenland Ministry of Energy, Utilities and Climate (GEUS) are used⁵¹.

Geological setting

Solution caves in Ordovician and Silurian partly dolomitized limestones are widespread across North Greenland, having formed as large phreatic systems beneath an uplifted coastal peneplain ~1,000 m asl. Apatite fission track analysis dates this uplift to ~10 Ma, coinciding with the older of two Miocene uplift phases in North-East Greenland and southern areas^{43,52}. Speleogenesis occurred concurrently with uplift, and in some locations, including the cave studied here, a small amount of vadose modification is evident as entrenchment and speleothem deposition^{23,33}. However, the lack of vadose modification or extensive speleothem deposits indicates that most caves did not transmit large volumes of water following phreatic drainage, thereby supporting the existence of cold-based ice sheets during Quaternary glaciations⁵⁴.

Cave sampling location

Flowstone samples (KC19-7, KC19-9, KC19-12 and KC19-14) were collected from the rear of Cove Cave (Eqik Qaarusussuaq; KC Cave) ~100 m from the entrance where cave air temperature in July 2019 was recorded at -14.0 ± 0.6 °C using an Extech RH300 digital hygro-thermometer²³. This spot cave air temperature measurement agrees within uncertainty with the MAAT from back trajectory analysis (-13.7 ± 1.0 °C). However, the contemporary cave morphology should not be considered as representative of when the analysed speleothems formed.

The sampling location contains a narrow vadose canyon, ~0.5 m wide and ~5 m deep (Extended Data Fig. 2). In situ flowstone drapes the palaeo-phreatic section and extends into the vadose canyon, indicating that vadose development predates speleothem deposition. Ex situ flowstone, presumed to have been broken through freeze–thaw processes, was sampled. KC19-7 was sampled from the extreme rear of the cave, at the top of the flowstone deposit, close to the roof. KC19-14 is a large broken curtain sequence sampled from the base of the flowstone sequence at the rear of the cave. Its original location could not be identified. It was cored due to its size. Before the vadose canyon, a boulder pile of broken speleothem was sampled ~15 m from KC19-7 and KC19-14. This pile yielded KC19-9 and KC19-12.

Petrography and mineralogy

The speleothem fabrics were assessed using thin sections under transmitted-light and blue-light epifluorescence microscopy. To determine the mineralogical composition of the white layer, approximately 45 mg of powder was hand-drilled from the white layer of KC19-7. A small aliquot of the homogenized (by mortar and pestle) powder was measured by X-ray diffractometry using a High-Resolution Powder Bruker-AXS D8-Discover at the Institute of Mineralogy and Petrography, University of Innsbruck. Phase identification was achieved with DIFFRAC.SUITE software and the PDF4+ (2024) database. Calcite was found to be the only phase.

Temperature reconstruction from reanalysis data

Greenland exhibits a large and abrupt temperature gradient from the continental interior to the coastline, particularly at the ice margin (Extended Data Fig. 3). Limited active monitoring near the study site inhibits precise characterization of local climate, because the nearest PROMICE weather stations (KPC-L and KPC-U) are located on the ice sheet, ~60–80 km southwest of KC Cave, and record a large temperature disparity (3.8 °C) over a short range (20 km). MAAT at KPC-L and KPC-U (from 2008 to 2023 CE) is -13.41 °C and -17.21 °C, respectively.

To estimate the 1991–2020 climatology at KC Cave, we obtained monthly 2-m temperatures from the fifth generation atmospheric

reanalysis from the European Centre for Medium-Range Weather Forecasts (ERA-5)⁵⁵, National Centers for Environmental Prediction and the National Center for Atmospheric Research (NCEP/NCAR)⁵⁶, and the Copernicus Arctic Regional Reanalysis (CARRA)⁵⁷ reanalysis datasets. Monthly means were calculated from CARRA's 6-hourly data. For each dataset, MAAT was derived using a two-dimensional interpolant of a 3×3 grid centred on the grid cell containing the cave. Lapse-rate adjustments were applied for the elevation difference between model output and the cave site (660 m asl) but had a negligible effect (<0.8 °C).

Monthly reanalysis data from ERA-5 and NCEP/NCAR exhibit cold biases between 4 °C and 5 °C when applied to stations KPC-L and KPC-U. However, the 2-m MAAT in CARRA was within 0.09 °C and 0.16 °C, of observed values at KPC-L and KPC-U, respectively (Extended Data Fig. 3). Thus, we have high confidence in the CARRA-based climatology for KC Cave (Extended Data Fig. 3), which yields a MAAT of -13.73 °C (1991–2020) and a recent warming rate of 0.89 ± 0.13 °C per decade.

Radiometric dating

Subsamples for U–Th dating were drilled in a thoroughly cleaned laminar flow hood used exclusively for low U concentration carbonate samples. Sample sizes ranged from 150 to 450 mg. Standard chemistry procedures were performed at the University of Minnesota to extract and purify U and Th aliquots⁵⁸. Samples were spiked with a dilute mixed ²²⁹Th–²³³U–²³⁶U tracer to correct for instrumental fractionation and calculate U and Th concentrations and ratios. Measurements were conducted on a Thermo-Finnigan Neptune multicollector inductively coupled plasma mass spectrometer⁵⁹ and ages calculated offline.

Laser ablation multi-collector inductively coupled plasma mass spectrometric (LA-MC-ICPMS) U–Pb dating was performed on highly polished slabs using laser ablation connected to a Thermo-Finnigan Neptune XT at the Institute of Global Environmental Change, Xi'an Jiaotong University⁶⁰. Samples were ultrasonically cleaned in deionized water to remove surface contamination. Samples and reference materials (RMs) were placed in an S155 cell (Laurin Technics 155, aerosol dispersion volume <1 cm³), and ablated using a 193 nm ArF LA system (RESolution LR). Aerosols were directly introduced into the LA-MC-ICPMS. Signal optimization used NIST616 and NIST614 glass, with conditions held constant during each run.

General parameters were 1.5–2.5 J cm⁻² at 100 μm spot size, 10 Hz for 25 s, with 5–15 preablation shots for surface cleaning. Every eight samples, NIST614 glass and carbonate RMs of known age^{60–62} were analysed to correct for instrument drift and matrix effects. Lolite software⁶³ was used for background subtraction, downhole effect correction and calculation of isotope ratios, errors, correlation coefficients and Tera–Wasserburg plots⁶⁴. U–Pb ages were calculated using IsoplotR⁶⁵.

The U/Pb ratio correction and U content (not strictly quantitative) were based on carbonate RMs ASH15⁶¹ and SB19-2⁶⁰. Initial disequilibrium corrections for ²³¹Pa, ²³⁰Th and ²²⁶Ra were omitted due to negligible effects in these old samples. ²³⁴U correction was also omitted, as its impact on young samples was <0.1 Ma—within error margins, especially when maximum error from RMs and mean square weighted deviation (MSWD) was applied. Furthermore, ²³⁴U values are not reliably known. Final reported errors for age and (²⁰⁷Pb/²⁰⁶Pb)₀ are two standard errors, including sample dispersion and RM uncertainty.

Age models were constructed using Bayesian modelling in Oxcal^{66,67}.

Stable isotope analysis

Stable isotope analysis was conducted at the University of Innsbruck. Speleothem samples for δ¹⁸O and δ¹³C analysis were micromilled at 250 μm resolution and analysed on a Thermo Fisher Scientific DeltaV isotope ratio mass spectrometer linked to GasBench II⁶⁸. In addition, 20 bedrock limestone samples were analysed, yielding δ¹⁸O values of -8.2 ± 0.3 ‰ and δ¹³C results of -0.1 ± 0.1 ‰ (2σ). All results are

reported relative to the NBS19 standard on the Vienna Peedee belemnite (VPDB) scale. Analytical precision was 0.08‰ for $\delta^{18}\text{O}$ and 0.06‰ for $\delta^{13}\text{C}$ (1 σ)⁶⁸.

Construction of the stacked composite stable isotope record

All four samples (KC19-7, KC19-9, KC19-12 and KC19-14) display comparable stable-isotope signals that, when cross-checked with macroscopic features (for example, petrographically inferred growth hiatuses and shared detrital-rich white layers), allow construction of a composite record and time series (Extended Data Fig. 5). Apart from the lower section of KC19-14 (118–200.4 mm), principal trends and perturbations are replicated in two to four samples across all intervals, with the strongest correlation between sample pairs KC19-7 versus KC19-9 and KC19-12 versus KC19-14 (Extended Data Fig. 5a–d). As KC19-14 contains the longest record (200.4 mm), it was used as the master record to construct the composite.

To combine the five micromilled tracks on a common depth scale, we tuned pairs of stable-isotope series using intrasite correlation age modelling (iscam) software in MatLab⁶⁹. Iscam parameters included 500 ARI simulations (each optimized with 1,000 Monte Carlo runs) and 10,000 Monte Carlo simulations of linearly interpolated age–depth models, with ages allowed to vary according to a Gaussian distribution.

Before input, synthetic ‘age models’ were created by treating 13–18 distinct isotopic, petrographic or macroscopic features in each pair as coeval events. Each event was assigned an ‘age’ corresponding to its depth in the master record and a 2σ uncertainty of 0.5 mm—twice the sampling resolution. KC19-7 was combined with its duplicate track to produce the KC19-7 composite, which was then tuned to KC19-9. KC19-12 was independently tuned to KC19-14, and the resulting pairwise composites were merged to form the master KC19 Composite $\delta^{18}\text{O}$ and $\delta^{13}\text{C}$ time series (Extended Data Fig. 5f, h, black lines) on a unified depth scale from 0 to 207.05 mm.

Individual iscam runs produced correlation coefficients (r) exceeding 0.9, and the robustness of the final composite is supported by strong replication of stable-isotope and elemental patterns across the shared depth scale (Extended Data Fig. 5f–h).

Major- and trace-element analysis by LA-ICP-MS

Analyses were performed in line-scan mode at the Institute of Geosciences, JGU Mainz, Germany, using an ESINWR193 ArF excimer laser ablation system with a TwoVol2 cell (193 nm wavelength), coupled to an Agilent 7700x quadrupole ICP-MS. Surfaces were preablated before each scan to remove surface contamination. Line scans were conducted at 15 $\mu\text{m s}^{-1}$ using a rectangular beam (130 \times 50 μm ; 150 \times 50 μm for preablation). The laser operated at 10 Hz with energy \sim 3.5 J cm⁻². Background intensities were recorded for 15 s. Monitored isotopes included ⁷Li, ²³Na, ²⁴Mg, ²⁵Mg, ²⁷Al, ³¹P, ³²S, ³⁴S, ³⁹K, ⁴⁴Ca, ⁴⁷Ti, ⁴⁹Ti, ⁵²Cr, ⁵³Cr, ⁵⁵Mn, ⁵⁶Fe, ⁵⁷Fe, ⁵⁹Co, ⁶⁰Ni, ⁶³Cu, ⁶⁶Zn, ⁷⁵As, ⁸⁵Rb, ⁸⁸Sr, ⁸⁹Y, ⁹⁰Zr, ⁹³Nb, ⁹⁵Mo, ¹¹¹Cd, ¹³³Cs, ¹³⁸Ba, ¹³⁹La, ¹⁴⁰Ce, ²⁰⁸Pb, ²³²Th and ²³⁸U.

Element concentrations were calibrated using synthetic glass NIST SRM 610 and preferred values from the GeoReM database^{70,71}. Quality control materials (QCMs)—USGS MACS-3, USGS BCR-2G and NIST SRM 612—monitored accuracy and precision. Signals were collected in time-resolved mode and processed with iolite4 software⁶³.

⁴³Ca was used as the internal standard, assuming a Ca concentration of 390,000 $\mu\text{g g}^{-1}$ for samples, and the corresponding GeoReM values for calibration materials and QCMs. Averaged element concentrations from repeated QCM measurements ($n = 15$) agreed within 10% of reference values⁷² (excluding ³²S and ⁵⁷Fe) and had a relative standard deviation (1RSD) <10%, except for P and S. Anomalous peaks were filtered by flattening >3 σ deviations from a locally weighted smoothing spline. Elemental data were then smoothed to match the stable-isotope sampling resolution using a 19-point locally estimated scatterplot smoothing (LOESS) before plotting and principal component analysis.

Trace element tracks relative to the stable isotope tracks are accurate to within 1 mm.

Modern $\delta^{18}\text{O}$ of meteoric precipitation

No station measuring precipitation isotopes exists near the field site. We therefore used data from the Global Network of Isotopes in Precipitation, specifically from Station Nord, Danmarkshavn, and Scoresby Sund on Greenland’s east coast. A latitudinal gradient was established between these sites, yielding an estimated value for the field site of -22.9‰ (mean) or -22.8‰ (weighted mean).

Correction of $\delta^{18}\text{O}$ for PCP

Prior calcite precipitation (PCP) along flow paths in the epikarst and cave system alters the residual karst-water composition of $\delta^{13}\text{C}$, $\delta^{18}\text{O}$ and certain elements (Mg, Sr, Ba and U), enriching values in secondary calcite above those produced by carbonate dissolution between CO₂-rich meteoric water and bedrock or soil^{73,74}. Isolating the time-varying PCP enrichment, particularly for $\delta^{18}\text{O}$, is key to reconstruct proxy signals reflecting climatic and environmental change, rather than in-cave processes.

We contend that pervasive enrichment of proxy data by PCP is evident through much of the KC19 record by: (1) an exceptional range in Mg concentration from 206 to 5,113 ppm, with most values falling above 920 ppm (Extended Data Fig. 5g); (2) broad covariance of Mg with Sr, Ba and U; (3) a statistically significant, positive covariance between $\ln(\text{Mg}/\text{Ca})$ and $\ln(\text{Sr}/\text{Ca})$ when Mg exceeds \sim 920 ppm (a positive ‘Sinclair test’), and; (4) the observation that eigenvectors for $\delta^{18}\text{O}$, Mg, Sr, Ba and U are nearly orthogonal to the trace-element suite associated with weathering and colloidal transport (Extended Data Fig. 8).

To back-calculate the $\delta^{18}\text{O}$ shift from PCP, we used the proxy system model⁷³, which simulates Rayleigh enrichment of Mg/Ca and $\delta^{18}\text{O}$ from assumed initial karst-water values until observed concentrations in speleothem calcite are matched. As this approach involves several simplifying assumptions, we caution that our PCP-corrected $\delta^{18}\text{O}$ series (Extended Data Fig. 8) reflect the maximum plausible enrichment, that is, the lowest likely $\delta^{18}\text{O}$ values of bicarbonate originally present in seepage water. First, initial $[\text{Mg}^{2+}]$ in karst water was calculated from the lowest observed speleothem value using a temperature-dependent partition coefficient. This assumes constant ground temperature and that minimum Mg/Ca represents PCP-free conditions. Second, the Mg partition coefficient is assumed independent of groundwater $[\text{Mg}^{2+}]$, although experiments show it decreases at higher concentrations⁷⁴. Third, aqueous $[\text{Ca}^{2+}]$ was estimated from site-specific controls on carbonate solubility, including temperature and soil $p\text{CO}_2$. Finally, we assume PCP alone caused Mg enrichment above the minimum. Although LA-ICP-MS Mg data were available only for KC19-7 and KC19-14, the high intersample consistency in both elemental and stable-isotope data supports extending the Mg/Ca signal to KC19-9 and KC19-12 on the shared depth scale.

To assess uncertainty in assumed initial conditions, we performed sensitivity tests by varying model parameters across a plausible range for the Miocene cave environment (Extended Data Fig. 8). Initial $[\text{Ca}^{2+}]$ had the greatest influence on $\delta^{18}\text{O}$ enrichment, as it directly affects calcite saturation and growth rate, modulating the extent of prior precipitation. Our median value of 1.84 mmol l⁻¹ corresponds to equilibrium calcite dissolution at \sim 5,000 ppm CO₂ in the soil–karst zone, comparable to modern mid- to high-latitude Eurasia⁷⁵. End-member values of 1.28 and 2.45 mmol l⁻¹ reflect \sim 1,500 and 15,000 ppm CO₂, respectively, unlikely but within observed ranges for Arctic/sub-Arctic biomes. However, at $[\text{Ca}^{2+}] < 1.84$ mmol l⁻¹, the model simulated unrealistically long PCP durations (>10,000 s) for high-Mg intervals, suggesting higher Ca²⁺ levels characterized the Miocene karst. The median cave temperature of 6 °C is consistent with Miocene warming, while end-member values of 1–15 °C span the plausible range. Water film

thickness was varied from 5 to 15 μm . These variations in temperature and film thickness had relatively minor effects on PCP-corrected $\delta^{18}\text{O}$.

The sensitivity test involved calculating PCP-corrected $\delta^{18}\text{O}$ series for all four samples using seven distinct parameter sets (Extended Data Fig. 8). These were merged on a common depth scale, and a 0.6-mm moving filter was applied to generate a kernel density function at each sampling depth. Although uncertainty reaches 3–4‰ in high-Mg intervals (for example, 48–106 mm depth), the main $\delta^{18}\text{O}$ trends and perturbations remain robust—except under unrealistically low initial $[\text{Ca}^{2+}]$ scenarios (1 and 2). The final PCP-corrected $\delta^{18}\text{O}$ composite (Extended Data Fig. 8e, black line) represents the median of the seven simulations across all samples and is interpreted as the primary meteoric water signal shaped by regional climatic variability. As incongruent calcite dissolution (ICD) can also cause similar cation covariance, we assessed it independently by examining temporal variance in Ba/Mg (Extended Data Fig. 9d). Dissolution experiments on the dolomitic limestone above Cove Cave (Eqik Qaarusussuaq) show ICD causes up to -10-fold Ba enrichment relative to Mg and Sr when dissolution is <1%, while Sr/Mg remains largely unchanged. We infer ICD is minimal or absent during high-Mg intervals, which reflect strong PCP enrichment, and is highest during low-Mg, high- $\delta^{18}\text{O}$ intervals—interpreted as the warmest and most humid periods.

Correction of $\delta^{13}\text{C}$ for PCP

Enrichment of $\delta^{13}\text{C}$ from PCP along flow paths is typically greater than that of $\delta^{18}\text{O}$ due to CO_2 outgassing during calcite precipitation⁷⁴. However, the $\delta^{13}\text{C}$ enrichment factor is more difficult to constrain due to greater sensitivity to initial conditions and high natural variability in the slope of $\delta^{13}\text{C}$ versus the fraction of residual $[\text{Ca}^{2+}]$ (fCa). Given these uncertainties, we did not construct a PCP-corrected $\delta^{13}\text{C}$ composite like for oxygen. Instead, we use the proxy system model by ref. 74 to assess the potential influence of PCP on $\delta^{13}\text{C}$ in the KC19 record. This model similarly assumes that the lowest Mg/Ca value reflects PCP-free conditions and applies a range of attenuation factors to the Mg partition coefficient to simulate reduced Mg uptake at elevated $[\text{Mg}^{2+}]$. A mid-range slope of -8‰ for $\delta^{13}\text{C}$ versus $\ln(\text{fCa})$ was used to evaluate the potential $\delta^{13}\text{C}$ effects.

In sample KC19-14, $\delta^{13}\text{C}$ ranges from -6.2‰ (5th percentile) to -1.8‰ (95th percentile), while Mg/Ca is generally anticorrelated, varying from 1.89 to 14.56 mmol mol^{-1} across the same percentiles. This Mg/Ca range suggests fCa values of 0.12–0.54 in the highest-Mg, lowest- $\delta^{13}\text{C}$ interval (-100–106 mm depth), yielding estimated initial (PCP-corrected) $\delta^{13}\text{C}$ values of -22.9‰ to -11.2‰. In the lowermost section (>165 mm depth), where $\delta^{13}\text{C}$ exceeds -4‰, fCa ranges from 0.15 to 0.95, giving initial $\delta^{13}\text{C}$ values of -19.4‰ to -2.2‰. Regardless of model assumptions, correcting for PCP amplifies the observed $\delta^{13}\text{C}$ trends, and thus does not alter the broader interpretations of this study.

Orbital parameters

The precision of astronomical calculations of Earth's orbital motion is considered reliable over the last 50 Ma (ref. 48). For the interval 9.6–9.0 Ma, obliquity phase uncertainty is estimated at ± 1.6 kyr (ref. 76). As in previous studies, eccentricity and obliquity have been combined to construct an eccentricity-tilt composite^{47,77}.

Northern North Atlantic SSTs

Although the text describes nNA SSTs 'relative to modern'^{5,18}, 'modern' as defined here has some nuances due to a lack of preindustrial calibration. 'Modern' therefore refers to a multidecade average from ocean atlases.

Data availability

Time-series stable isotope and trace element data are available via the National Centers for Environmental Information National Oceanic and

Atmospheric Administration at <https://doi.org/10.25921/z522-b765> (ref. 78). All other data are provided with the Article.

References

- Dawes, P. R., Glendal, E. W. & Holst, J. A *Glossary for GEUS Publications: Spelling and Usage of Troublesome Words and Names Made Easy 74* (Geological Survey of Denmark and Greenland Ministry of Energy, Utilities and Climate, 2016).
- Japsen, P., Green, P. F. & Chalmers, J. A. Thermo-tectonic development of the Wandel Sea Basin, North Greenland. *GEUS Bull.* **45**, 5298 (2021).
- Smith, P. & Moseley, G. The karst and palaeokarst of North and North-East Greenland—physical records of cryptic geological intervals. *GEUS Bull.* **49**, 8298 (2022).
- Lane, T. P. et al. The geomorphological record of an ice stream to ice shelf transition in Northeast Greenland. *Earth Surf. Process. Landf.* **48**, 1321–1341 (2023).
- Hersbach, H. et al. *ERA5 monthly averaged data on single levels from 1940 to present* (Copernicus Climate Change Service (C3S) Climate Data Store, 2023).
- Kalnay, E. et al. The NCEP/NCAR 40-Year Reanalysis Project. *Bull. Am. Meteorol. Soc.* **77**, 437–472 (1996).
- Schyberg, H. et al. *Arctic Regional Reanalysis on Single Levels from 1991 to Present*. (Copernicus Climate Change Service (C3S) Climate Data Store (CDS), 2021).
- Edwards, L. R., Chen, J. H. & Wasserburg, G. J. ^{238}U ^{234}U ^{230}Th ^{232}Th systematics and the precise measurement of time over the past 500,000 years. *Earth Planet. Sci. Lett.* **81**, 175–192 (1987).
- Shen, C.-C. et al. High-precision and high-resolution carbonate ^{230}Th dating by MC-ICP-MS with SEM protocols. *Geochim. Cosmochim. Acta* **99**, 71–86 (2012).
- Jian, W. et al. U-Pb dating of Quaternary speleothems using LA & ID MC-ICPMS. *Quat. Sci.* **42**, 1410–1419 (2022).
- Nuriel, P. et al. The use of ASH-15 flowstone as a matrix-matched reference material for laser-ablation U-Pb geochronology of calcite. *Geochronology* **3**, 35–47 (2021).
- Hill, A. C., Polyak, J. V., Asmerom, Y. & Provencio, P. P. Constraints on a Late Cretaceous uplift, denudation, and incision of the Grand Canyon region, southwestern Colorado Plateau, USA, from U-Pb dating of lacustrine limestone. *Tectonics* **35**, 896–906 (2016).
- Paton, C., Hellstrom, J., Paul, B., Woodhead, J. & Hergt, J. lolite: freeware for the visualisation and processing of mass spectrometric data. *J. Anal. Spectrom.* **26**, 2508 (2011).
- Tera, F. & Wasserburg, G. J. U-Th-Pb systematics in three Apollo 14 basalts and the problem of initial Pb in lunar rocks. *Earth Planet. Sci. Lett.* **14**, 281–304 (1972).
- Vermeesch, P. IsoplotR: a free and open toolbox for geochronology. *Geosci. Front.* **9**, 1479–1493 (2018).
- Ramsey, C. B. Deposition models for chronological records. *Quat. Sci. Rev.* **27**, 42–60 (2008).
- Ramsey, C. B. & Lee, S. Recent and planned developments of the program OxCal. *Radiocarbon* **55**, 720–730 (2013).
- Spötl, C. Long-term performance of the Gasbench isotope ratio mass spectrometry system for the stable isotope analysis of carbonate microsamples. *Rapid Commun. Mass Spectrom.* **25**, 1683–1685 (2011).
- Fohlmeister, J. A statistical approach to construct composite climate records of dated archives. *Quat. Geochronol.* **14**, 48–56 (2012).
- Jochum, P. K. et al. GeoReM: a new geochemical database for reference materials and isotopic standards. *Geostand. Geoanal. Res.* **29**, 333–338 (2005).
- Jochum, P. K. et al. Determination of reference values for NIST SRM 610–617 glasses following ISO guidelines. *Geostand. Geoanal. Res.* **35**, 397–429 (2011).

72. Jochum, P. K. et al. Accurate trace element analysis of speleothems and biogenic calcium carbonates by LA-ICP-MS. *Chem. Geol.* **318–319**, 31–44 (2012).
73. Skiba, V. & Fohlmeister, J. Contemporaneously growing speleothems and their value to decipher in-cave processes—a modelling approach. *Geochim. Cosmochim. Acta* **348**, 381–396 (2023).
74. Stoll, M. H. et al. Distinguishing the combined vegetation and soil component of $\delta^{13}\text{C}$ variation in speleothem records from subsequent degassing and prior calcite precipitation effects. *Climate* **19**, 2423–2444 (2023).
75. Goncharova, Y. O., Timofeeva, V. M. & Matyshak, V. G. Carbon dioxide in soil, ground and surface waters of the northern regions: role, sources, test methods (a review). *Eurasia Soil Sci.* **56**, 278–293 (2023).
76. Zeeden, C., Hilgen, J. F., Hüsing, K. S. & Lourens, L. L. The Miocene astronomical time scale 9–12 Ma: new constraints on tidal dissipation and their implications for paleoclimatic investigations. *Paleoceanography* **29**, 296–307 (2014).
77. Holbourn, A. E. et al. Late Miocene climate cooling and intensification of southeast Asian winter monsoon. *Nat. Commun.* **9**, 1584 (2018).
78. Moseley, G. E. et al. Eastern North Greenland Speleothem $\delta^{18}\text{O}$, $\delta^{13}\text{C}$, Trace Element Data 5.3 to 9.5 Myr. *National Centers for Environmental Information* <https://doi.org/10.25921/z522-b765> (2025).
79. How, P. et al. *PROMICE and GC-Net Automated Weather Station Data in Greenland* (GEUS Dataverse, 2022).
80. McDonough, W. F. & Sun, S.-S. The composition of the Earth. *Chem. Geol.* **120**, 223–253 (1995).
81. Pedersen, M. & Hansen, M. *The One-stop Shop to Geoscience Data from Greenland*: www.greenmin.gl. Exploration and mining in Greenland Fact Sheet No. 33 (GEUS, 2018).
82. Estrada, S., Tessensohn, F. & Sonntag, B.-L. A Timanian island-arc fragment in North Greenland: the Midtkap igneous suite. *J. Geodyn.* **118**, 140–153 (2018).
83. Kalsbeek, F., Jepsen, F. H. & Jones, A. K. Geochemistry and petrogenesis of S-type granites in the East Greenland Caledonides. *Lithos* **57**, 91–109 (2001).
84. Kalsbeek, F. & Jepsen, H. F. The Midsommersø dolerites and associated intrusions in the proterozoic platform of eastern North Greenland—a study of the interaction between intrusive basic magma and sialic crust. *J. Petrol.* **24**, 605–634 (1983).
- Comer Science and Education Foundation (CP108), Petzl Foundation, Mount Everest Foundation (15-04), Austrian Academy of Sciences, British Cave Research Association, Transglobe Expedition Trust, National Speleological Society, Quaternary Research Association, Wilderness Lectures and Ghar Parau Foundation. Thanks to the Greenland government for permission (KNNO Expedition Permit C-19-32; Scientific Survey Licence VU-00150; Greenland National Museum and Archives 2019/01) and to S. R. Rasmussen (Polog), Norlandair, and Air Greenland for logistics. Thanks to V. Skiba, M. Wimmer, R. Mertz, T. Leger, A. Baldo, A. Crisitiello and P. Markwisch for discussions, analyses and data. Participants in the 2019 Greenland Caves Expedition included H. Barton, S. E. Bjerkenås, C. Blakeley, P. Hodgkinson, A. Ignézi, R. Shone, H. C. Sivertsen, A. Sole and P. Töchterle.

Author contributions

GEM: conceptualization and research design, fund acquisition, expedition planning, field methodology, permit acquisition, analytical methodology, data acquisition, supervision, project administration, data analysis, visualization, and writing – original draft, review and editing. G.K. and J.L.B.: analytical methodology, data acquisition, data analysis, visualization, and writing – review and editing. J.W.: analytical methodology, data acquisition and data analysis. H.S., M.P.S., C.S., A.H. and C.J.: resources, data acquisition, and writing – review and editing. A.D. and L.F.: data acquisition. H.S., H.C. and R.L.E.: resources and data acquisition.

Funding

Open access funding provided by University of Innsbruck and Medical University of Innsbruck.

Competing interests

The authors declare no competing interests.

Additional information

Extended data is available for this paper at <https://doi.org/10.1038/s41561-025-01822-0>.

Supplementary information The online version contains supplementary material available at <https://doi.org/10.1038/s41561-025-01822-0>.

Correspondence and requests for materials should be addressed to Gina E. Moseley.

Peer review information *Nature Geoscience* thanks Ruediger Stein and the other, anonymous, reviewer(s) for their contribution to the peer review of this work. Primary Handling Editor: James Super, in collaboration with the *Nature Geoscience* team.

Reprints and permissions information is available at www.nature.com/reprints.

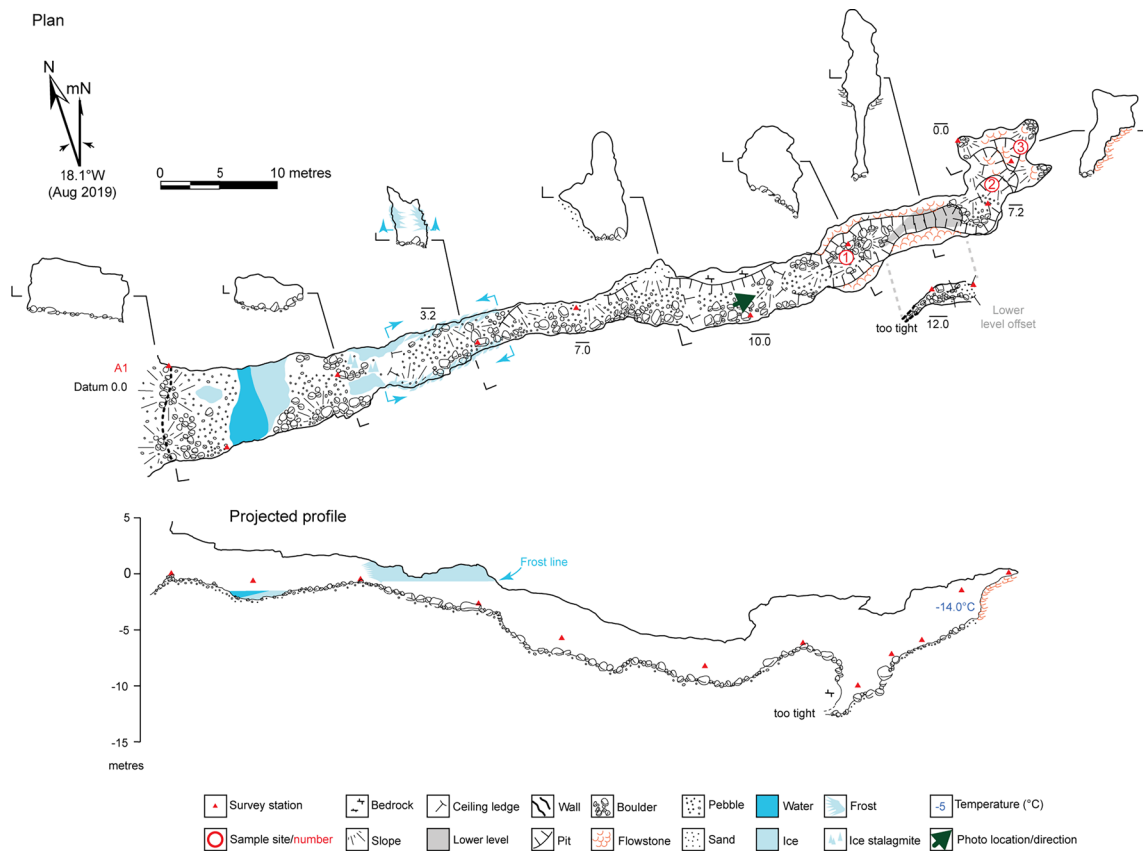
Acknowledgements

This research was funded by the Austrian Science Fund (FWF) (10.55776/Y1162) (G.E.M.). For open-access purposes, we have applied a CC BY public copyright licence to any author-accepted manuscript version arising from this submission. Additional support to G.E.M. came from the Rolex Award for Enterprise, National Geographic Society (9638-15), University of Innsbruck Nachwuchsförderung,

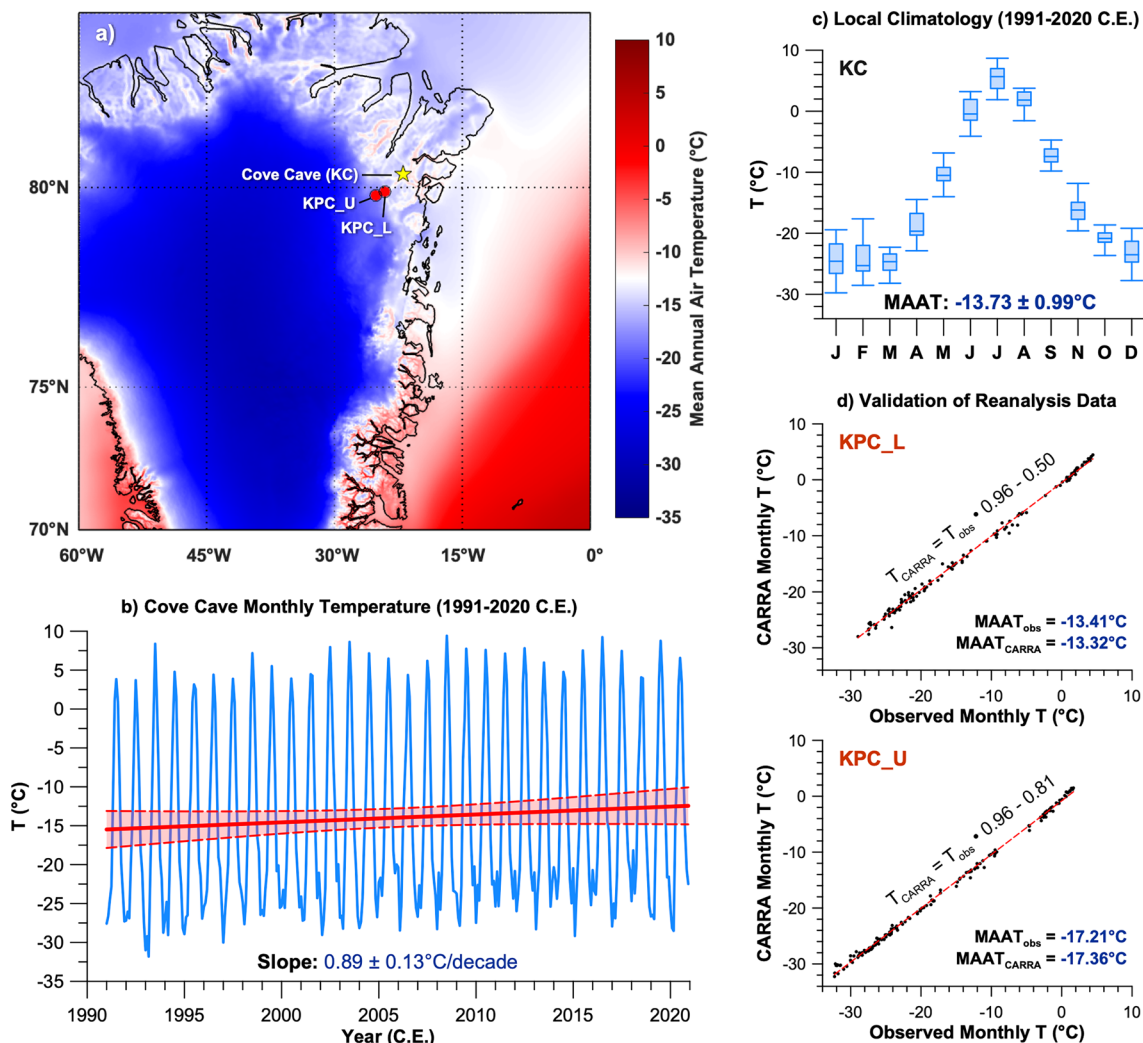


Extended Data Fig. 1 | Field location of Cove Cave (Eqik Qaarusussuaq). **a**, Steep-sided canyon with surface river flowing in base. **b**, Thin cryptobiotic soils on the valley floor in Grottedalen displaying patterned ground from the action of permafrost. **c**, Cave entrance with people for scale and helicopter in the valley.

This valley is a small hanging tributary valley to (a), d, Vadose canyon (below figure in background) at the rear of the cave. Flowstone samples were collected from either side of the canyon. See Extended Data Fig. 2 for photo location. Credit: **a,b,d**, Robbie Shone; **c**, Andrew Sole.

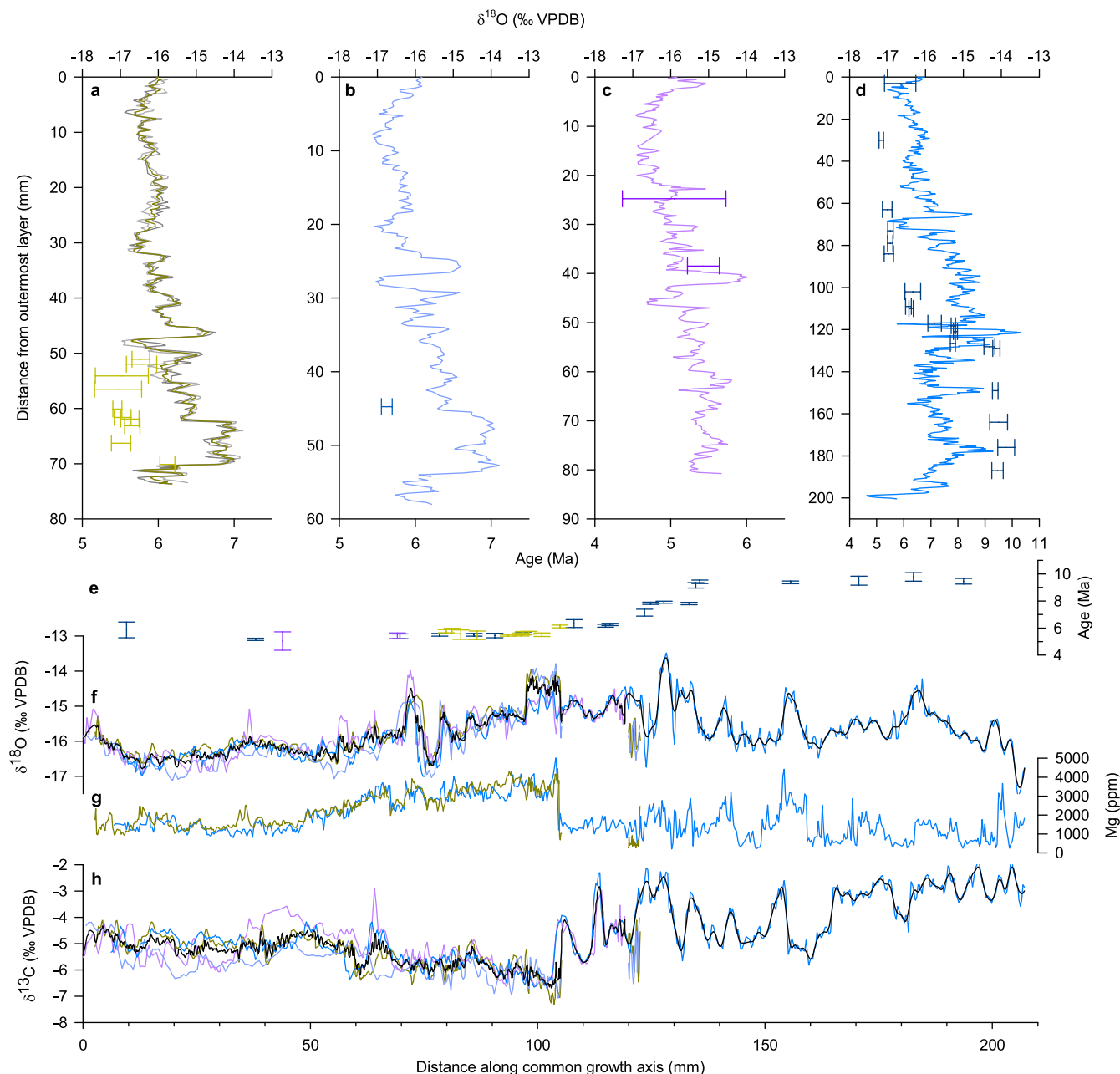


Extended Data Fig. 2 | Survey of Cove Cave (Eqik Qaarussuaq). Adapted from²³. Samples were collected as follows: 1, KC19-9 and KC19-12, 2, KC19-14, 3, KC19-7. The position of the photo refers to Extended Data Fig. 1d. Figure adapted from ref. 23 under a Creative Commons license [CC BY](https://creativecommons.org/licenses/by/4.0/).



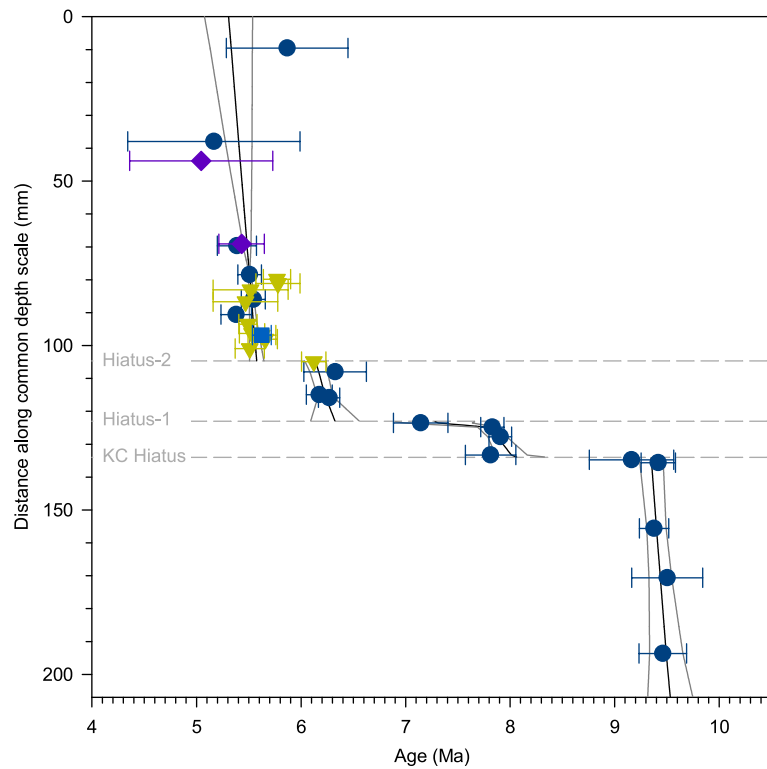
Extended Data Fig. 3 | Mean 2 m air temperature at the field site in eastern North Greenland (Kalaallit Nunaat). **a**, Mean 2 m air temperature 1991-2020 as reconstructed from the Copernicus Arctic Regional Reanalysis dataset⁵⁷. The cave site is marked KC. Weather stations of the Programme for Monitoring of the Greenland Ice Sheet & Greenland Climate Network⁷⁹ are marked KPC_L and KPC_U. **b**, Monthly surface temperature at the cave site in the Copernicus

Arctic Regional Reanalysis dataset. **c**, Recent climatology (1991–2020) for the cave site and estimated mean annual air temperature. Box and whisker plots for individual months ($n = 30$). Boxes indicate median and interquartile range (25–75th percentile); whiskers denote 5–95th percentile range. **d**, Reanalysis data in the Copernicus Arctic Regional Reanalysis dataset validated from nearest weather stations.



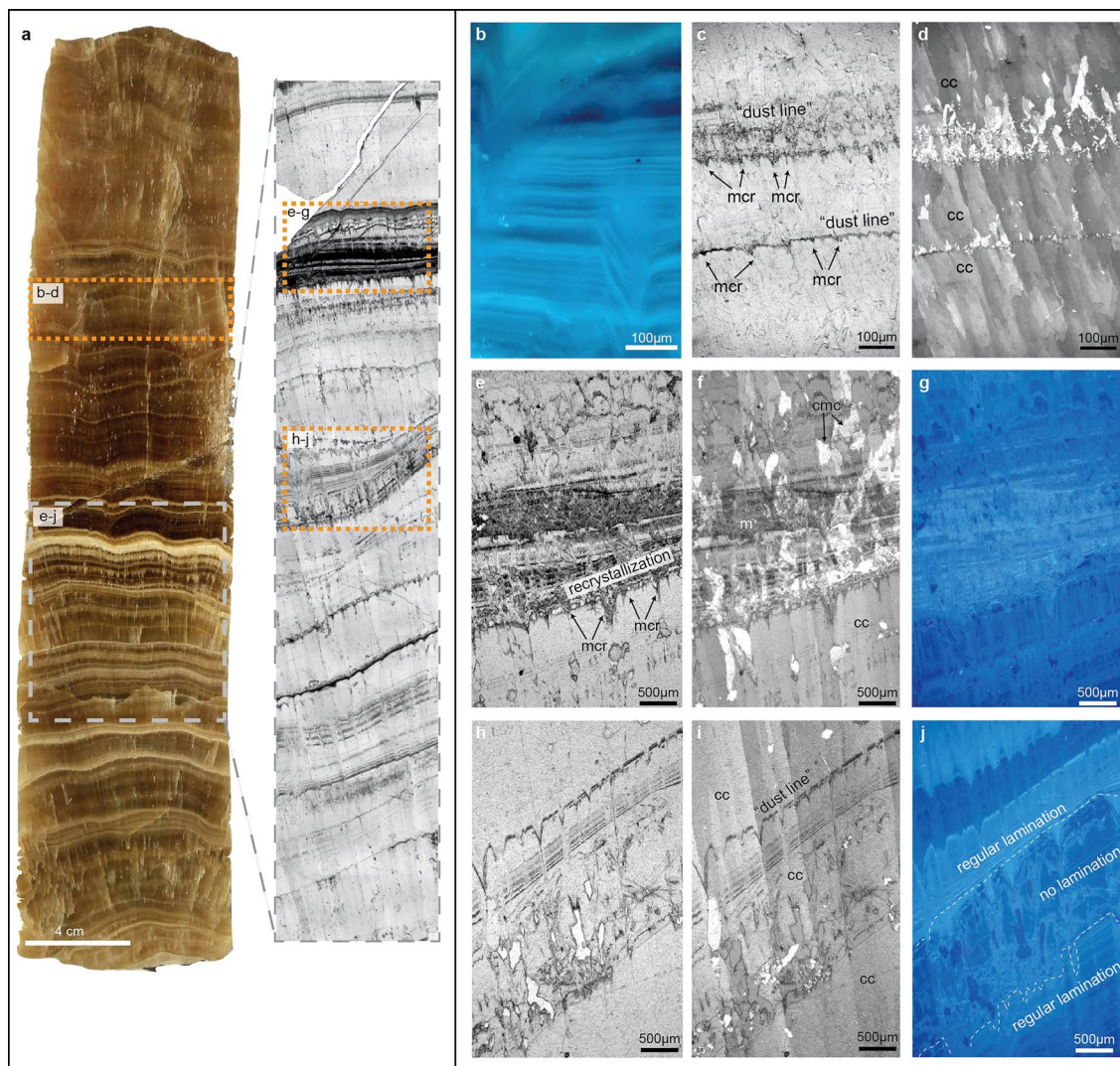
Extended Data Fig. 5 | Reproducibility of records and construction of the common depth scale. **a**, KC19-7 $\delta^{18}\text{O}$ isotope track 1 (light grey); KC19-7 $\delta^{18}\text{O}$ isotope track 2 (dark grey); KC19-7 $\delta^{18}\text{O}$ composite record of KC19-7 tracks 1 and 2 (dark yellow). U-Pb ages plotted as mean and propagated 2 standard error (light yellow bars with caps). Individual statistics given in Supplementary Table 1. **b**, KC19-9 $\delta^{18}\text{O}$ (light blue). U-Pb ages plotted as mean and propagated 2 standard error (medium blue bars with caps). Individual statistics given in Supplementary Table 1. **c**, KC19-12 $\delta^{18}\text{O}$ (light purple). U-Pb ages plotted as mean and propagated 2 standard error (medium purple bars with caps). Individual

statistics given in Supplementary Table 1. **d**, KC19-14 $\delta^{18}\text{O}$. U-Pb ages plotted as mean and propagated 2 standard error (dark blue bars with caps). Individual statistics given in Supplementary Table 1. **e**, All ages with a 2-sigma uncertainty range given on the common depth scale. Colours same as for **a-d**. **f**, $\delta^{18}\text{O}$ records on the common depth scale. KC19-7_{composite} (yellow); KC19-9 (light blue); KC19-12 (light purple); KC19-14 (medium blue). Composite stacked $\delta^{18}\text{O}$ record (black). **g**, Mg concentration of KC19-7 (yellow) and KC19-14 (medium blue). **h**, As for **e** but for $\delta^{13}\text{C}$.



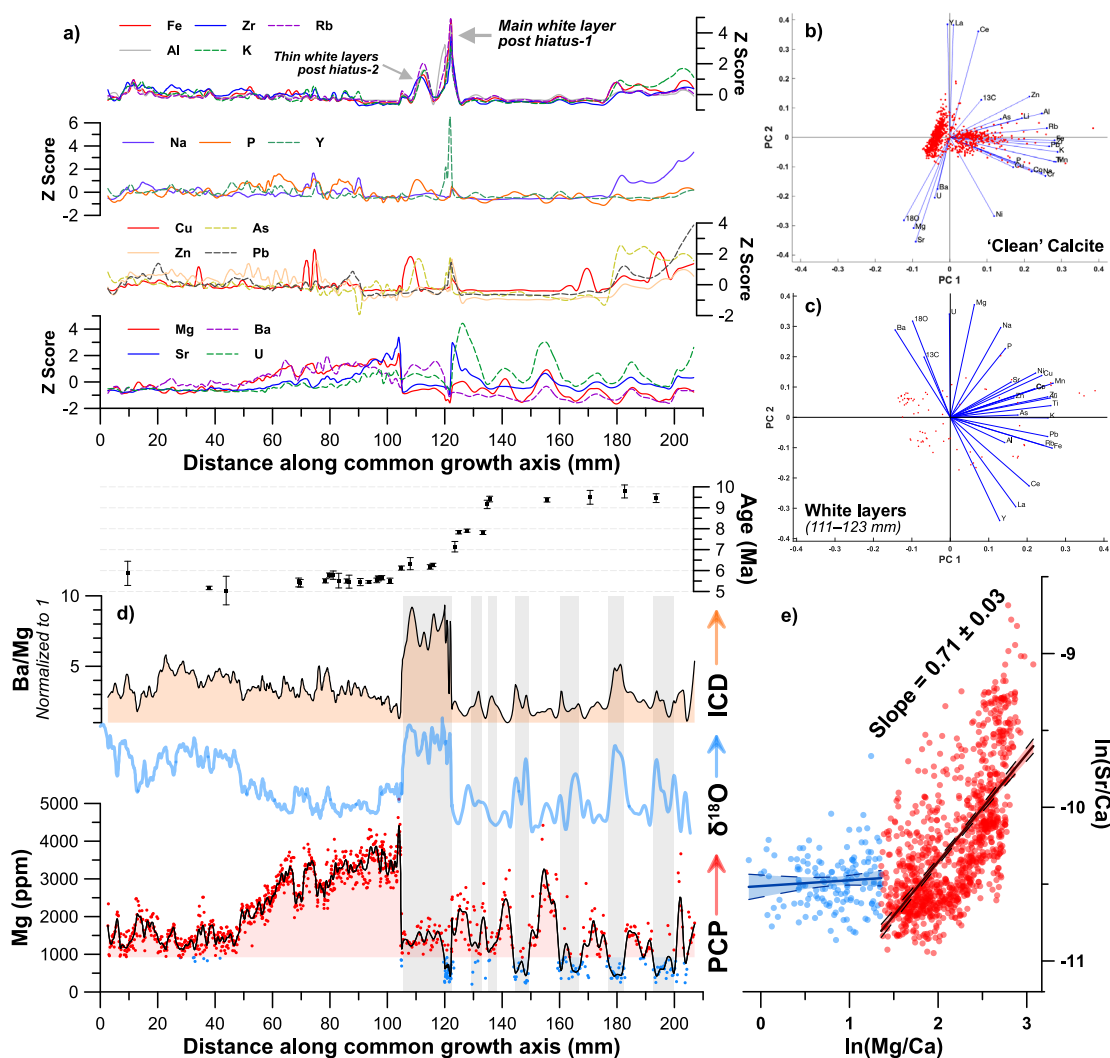
Extended Data Fig. 6 | The age model for the composite stacked record constructed in OxCal^{66,67}. KC19-7 (yellow triangles), KC19-9 (light blue squares), KC19-12 (purple diamonds), KC19-14 (medium blue circles). U-Pb ages plotted as mean and propagated 2 standard error. Individual statistics given in

Supplementary Table 1. The solid black line indicates the central age model. Solid grey lines indicate 2-sigma uncertainty on the age model. Horizontal grey dashed lines indicate the position of hiatuses.



Extended Data Fig. 7 | Thin section photomicrographs of KC19-14. **a**, Main slab of KC19-14 and a panoramic view of a thin section showing the areas of photomicrographs **b-d** and **e-j** (orange dashed rectangles), respectively. **b**, Semi-regular fluorescent lamination seen under UV. **c**, Thin “dust lines” rich in opaque inclusions mark possible growth hiatuses in plane-polarised light. **d**, The same section under cross-polarised light, showing laterally discontinuous interruption of columnar crystal growth. **e** to **g** are thin section images of hiatus-1 (as defined

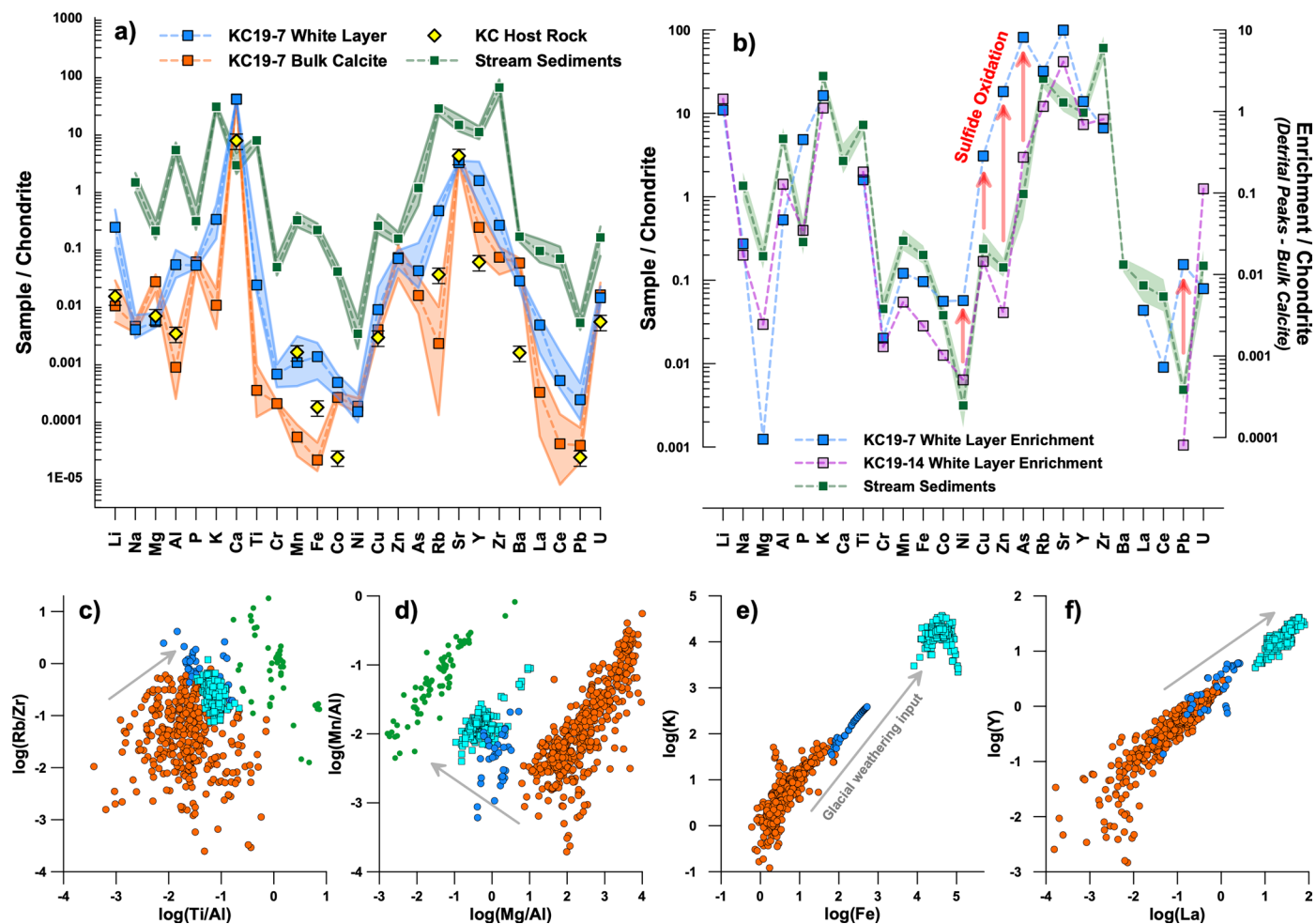
in main text, see Extended Data Fig. 6), showing a sharp transition from columnar calcite below to micritic calcite above. **h** to **j** are thin section images of ‘KC-hiatus’ (as described in main text, see Extended Data Fig. 6), showing columnar calcite fabric. Ultraviolet fluorescence reveals a ca. 1.5 mm-thin zone lacking regular fluorescent lamination. The micritic zone shows brighter epifluorescence than the columnar calcite. cc: columnar calcite, cmc: columnar microcrystalline calcite, m: micrite, mcr: micro-corrosion.



Extended Data Fig. 8 | Major and trace elements of KC19-7 and KC19-14.

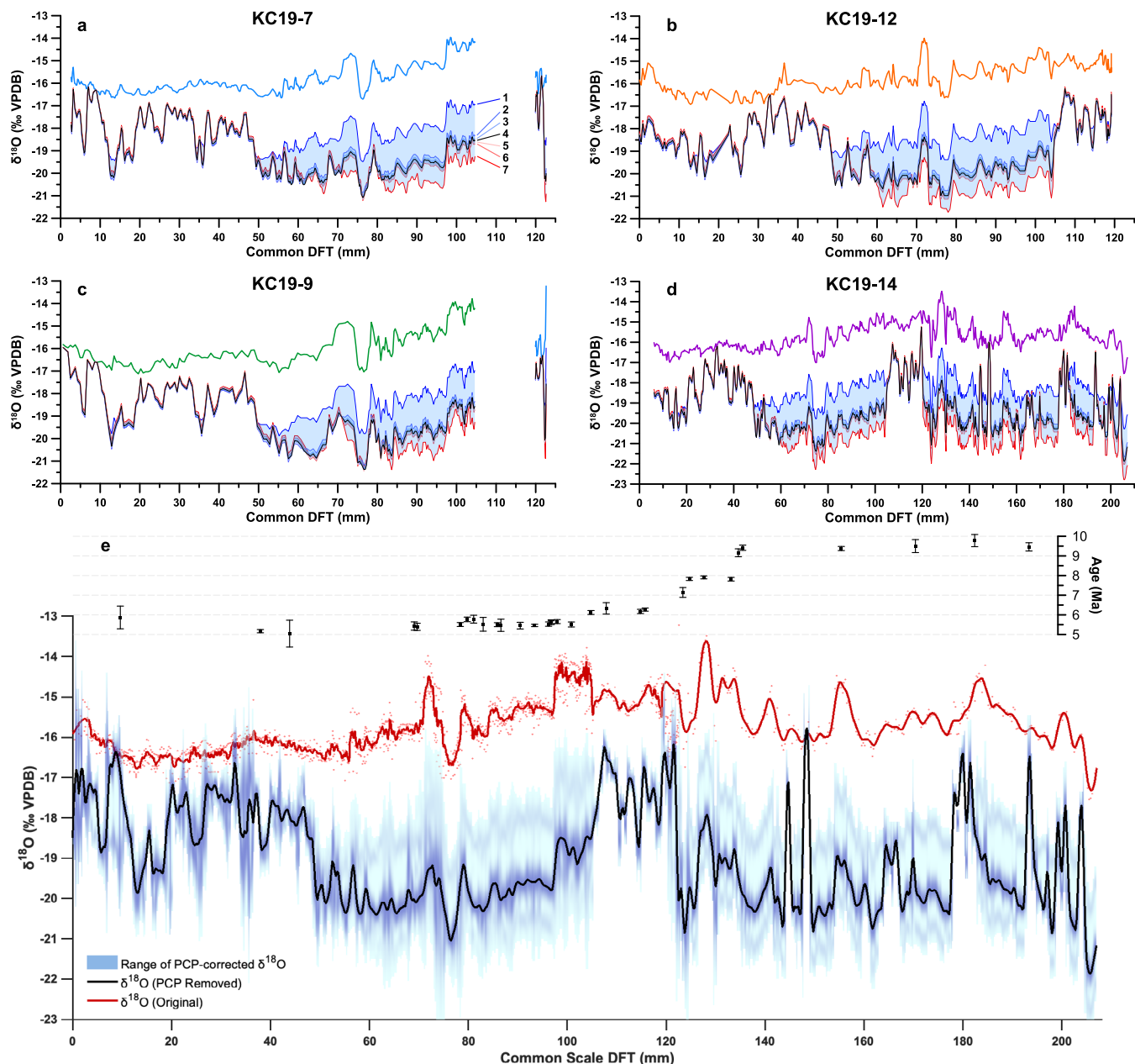
a, Selected elements associated with silicate weathering (Fe, Zr, Rb, Al, K), sea spray (Na) and colloidal soil transport (P, Y), sulphide oxidation (Cu, As, Zn, Pb), and prior calcite precipitation (PCP; Mg, Sr, Ba, U). Data standardised to Z-scores for comparison. Z scores calculated as standard deviation units of each time series ($n = 1179$), $Z = (x_i - \mu) / \sigma$. **b**, Principal component 1 and 2 scores for the bulk calcite (excluding detrital-rich white layer). **c**, Principal component 1 and 2 scores for detrital-rich white layer. **d**, U-Pb ages (2-sigma uncertainty) on

common depth scale plus proxies for enhanced incongruent calcite dissolution (Ba/Mg, normalised to the lowest value) and for prior calcite precipitation (Mg; values above/below -920 ppm in red/blue). Grey bars show intervals of enhanced incongruent calcite dissolution and reduced prior calcite precipitation during warm climates, inferred from prior calcite precipitation-corrected $\delta^{18}\text{O}$. **e**, 'Sinclair Test' for prior calcite precipitation enrichment of Mg and Sr, positive only when Mg exceeds -920 ppm.



Extended Data Fig. 9 | Glacial provenance of white layer trace-element enrichment. **a**, Spider diagram of C1 chondrite-normalised⁸⁰ elemental concentrations of the brown calcite (orange) and distinct white layer (blue) in sample KC19-7, compared to the carbonate host rock (yellow) and a compilation of modern, glacially discharged stream sediment samples⁸¹ (green) within ~100 km of KC Cave (Eqik Qaarusussuaq). Bedrock values (yellow diamonds) plotted as the arithmetic mean of triplicate measurements, error bars show $\pm 30\%$. Dashed lines and shading indicate median and interquartile range (25–75th percentile) of KC19-7 bulk calcite ($n = 502$), white layer ($n = 35$), and stream sediments ($n = 300$). **b**, Spider diagram showing the composition of trace-element enrichment within the distinct white layer of KC19-7 (blue) and KC19-14 (pink), compared to the composition of stream sediments. To quantify

trace-element enrichment, we applied the same normalisation to the difference (in ppm) between white layer peaks and bulk calcite values. Red arrows highlight the enhanced enrichment of sulphide-associated metals. Shading in **a** and **b** shows the interquartile range of respective datasets. **c**, **d**, **e**, **f**, cross plots of common proxies for detrital provenance in a log-log space, illustrating mixing between local carbonate host rock (captured by the brown calcite, orange circles) and glacially discharged stream sediments (light blue squares) to produce the composition of the white layer (blue circles). Green dots in **c** and **d** show the composition of igneous emplacements and siliciclastic sequences within the Ellesmerian and Caledonian deformation belts of North and East Greenland^{82–84}, far more distal from KC Cave (Eqik Qaarusussuaq).



Extended Data Fig. 10 | Removal of prior calcite precipitation effect from measured $\delta^{18}\text{O}$. Measured $\delta^{18}\text{O}$ in **a**, KC19-7 (blue), **b**, KC19-12 (orange), and **d**, KC19-14 (purple), corrected for the ^{18}O -enrichment from prior calcite precipitation⁷³. Parameters for $p\text{CO}_2$, temperature (T), and water film thickness (D) were varied in 7 scenarios to conduct a sensitivity test of the model: 1 · $p\text{CO}_2 = 1500$ ppm; T = 1 °C; D = 0.015 mm; 2 · $p\text{CO}_2 = 3550$ ppm; T = 1 °C; D = 0.01 mm; 3 · $p\text{CO}_2 = 4370$ ppm; T = 4 °C; D = 0.01 mm; 4 · $p\text{CO}_2 = 5000$ ppm; T = 6 °C; D = 0.01 mm; 5 · $p\text{CO}_2 = 5750$ ppm; T = 8 °C; D = 0.01 mm; 6 · $p\text{CO}_2 = 7080$

ppm; T = 11 °C; D = 0.01 mm; 7 · $p\text{CO}_2 = 15000$ ppm; T = 15 °C; D = 0.005 mm. **e**, U-Pb ages plotted as mean and propagated 2 standard error on common depth scale. Individual statistics given in Supplementary Table 1. Composite of measured $\delta^{18}\text{O}$ data for all KC samples (red). Normalised kernel density function (blue shading) of prior calcite precipitation-corrected $\delta^{18}\text{O}$, estimated from all model outputs with parameters in scenarios 1-7 and using a 0.6-mm window to account for unequal sampling resolutions. The bold black line shows the maximal probability at each step. DFT = distance from top.